Determination of the Image Distance in a Plenoptic Camera

by

Chelsea Thomason

A thesis submitted to the Graduate Faculty of
Auburn University
in partial fulfillment of the
requirements for the Degree of
Master of Science

Auburn, Alabama
December 13, 2014

Keywords: plenoptic, refraction, calibration

Approved by

Brian Thurow, Chair, Associate Professor of Aerospace Engineering
Stan Reeves, Professor of Electrical and Computer Engineering
Joseph Majdalani, Department Head of Aerospace Engineering

Abstract

Two methods for determining the distance between the lens of a plenoptic camera and the focal plane, known as the image distance, are presented and tested. The plenoptic camera is a form of light field imaging, which seeks to record both the spatial and angular information of the light within a volume. The plenoptic camera requires one calibration image to determine the location of the focal points of each microlens within the camera. The focal point method of calibration uses the location of these focal points to geometrically determine the image distance. The magnification method of calibration instead requires an additional calibration image of a ruler and uses the standard, well-studied imaging equations to back out this distance. This thesis seeks to analyze both methods of calibration for accuracy and robustness across a wide range of possible image distances. The magnification method is proven to provide a sound estimation for the image distance for all of the tested cases. Synthetic results show that the focal point method of calibration is mathematically sound, but experimental results show that the real application of the method is limited by several deficiencies, namely errors caused by assuming that a complex lens exhibits the same properties as a thin lens. Results show that the focal point method can provide comparable accuracy to the magnification method by applying a correction equation specific to each lens settings, but overall the magnification is more robust and much simpler for general experiments.

Acknowledgments

First, I would like to thank Dr. Brian Thurow for being willing to discuss and work through all the complications that arose from this study in the countless hours I have spent in his office. His insight led to most, if not all, of the major discoveries throughout this thesis work.

I would also like to thank my parents for supporting me immensely throughout these past two and a half years, and for always being understanding when I had to write during the holidays.

Most importantly, I want to thank God for giving me the strength to make it through this process, especially during these past three months.

Table of Contents

List of Figures

List of Tables

Chapter 1

Introduction

Plenoptic particle image velocimetry (PIV) is being explored to address current limitations in PIV imaging. PIV, introduced by Adrian in 1984 [1], is an imaging method that seeds a flow with minuscule particles that scatter all light impinging on each particle. A desired region of this flow is then illuminated by a thin sheet of light, typically a laser, and imaged with a single camera. The cameras that are used with PIV are designed with a high frame rate, such that two images may be taken sequentially within a fraction of a second. The distance the particles shift between the two images is then measured and divided by the time step to determine the two-dimensional velocity field of the flow [2]. While the premise behind this technique remains true in current implementations, there have been many advancements in not only the accuracy of the imaging systems but also in the dimensions and resolutions of the results.

The concept of using multiple cameras to ascertain the depth component of velocity has been used in experiments for decades, but the first to introduce a dual-camera system to PIV, named stereoscopic PIV (stereo-PIV), was Arroyo and Greated in 1991 [3]. In stereo-PIV, each camera is placed at a different angle with respect to the particle field, thus allowing the depth component to be determined and subtracted from the in-plane components of velocity. This reduces the error in the two-dimensional velocity field caused by out-of plane motion. By combining a single PIV camera with a stereo-PIV system, the accuracy can be improved even more. Raffel proposed placing these systems to view perpendicular planes to best estimate the out-of-plane component [4], but Ganapathisubramani showed that a three-dimensional volume could be reconstructed by placing these systems in parallel planes [5]. In the same way, two stereo-PIV systems can be combined to form a dual-plane stereo-PIV imaging

system [6]. One of the more recent advances, tomographic PIV (tomo-PIV) expands the laser sheet into a volume and utilizes four or more cameras viewing the illuminated volume, from which the full volume may be reconstructed in a computationally-intensive process [7]. Similarly, synthetic aperture PIV (SAPIV) uses even more cameras, typically eight or more, in a tight cluster to image and reconstruct a volume. Although more cameras are used, the reconstruction process is much faster than the tomographic counterpart[8]. With each additional camera, however, more and more optical access to the flow is required to fully capture the three-dimensional information.

Along the same lines, several single camera systems have been developed to determine the three-dimensional properties of a volume. The first of such systems was presented by Willert in 1997. This camera determines the depth of a particle by placing three pinholes across the lens of the camera and using the principle of defocusing. While capable of producing three-dimensional results, this method only permits a limited number of particles to be seeded into the flow [9]. In contrast to using multiple cameras to view different planes, another method named scanning PIV captures a volume by moving the laser sheet through the area and records these multiple planes onto the same camera or camera systems [10, 11]. Holographic PIV can be used to combine light rays reflected off the particles in a flow with a reference beam to make an inference pattern onto a sensor [12, 13]. The volume can then be reconstructed from this image with a high spatial resolution, and eliminates the restriction caused by the lens of a camera. This method, however, is best reserved for small-scale experiments [2].

Despite the large number of possible camera combinations and imaging techniques, there remain several types of flow configurations that current PIV techniques cannot adequately image, such as the regime of highly turbulent flows with limited optical access. Single camera systems require minimal optical access to acquire measurements, but either provide only two-dimensional results that are insufficient for a fully three-dimensional turbulent flow, or have limitations in particle density that would limit the resolution of the results. While multiple

camera systems can back out the three-dimensional properties of a flow, each camera must have a unique view of the flow in question. For cases such as combustion gas ignition, where the high temperatures restrict the size of a glass viewing panel, or porous flow, where the porous solid model can hinder imaging, an imaging system consisting of a single camera capable of producing three-dimensional results is necessary.

The imaging technique known as light-field imaging is an emerging technology that may provide the solution to this limitation in PIV. Light is known to propagate in all dimensions from every point in space, defined by three spatial components (x, y, z) and two angular components (θ, ϕ). Conventional cameras only record two of these five dimensions of the light passing through a camera. The goal of light field imaging is to record not only the spatial location of where light impacts the image sensor, but also the angle of incidence. By including these additional two dimensions, the depth of the origin of the light z can be obtained. One camera that has been introduced to photography within the past fifteen years has the capability to record all four of these dimensions onto a single image sensor. This camera, known as the plenoptic camera, is adapted from a conventional camera by placing an area of small, micrometer-sized lenses in front of the image sensor [14]. With this small change, the light striking each microlens is divided among the pixels beneath each microlens depending on the angle of incidence of the light. This retention of angular data allows the depth of the imaged objects to be ascertained, all from a single image. While the plenoptic camera has been well-proven in general photography, only within the past five years has this system begun to be tested as a candidate for the next leading method of PIV [15, 16]; furthermore, this camera has the potential to image several fluid flows that are unobtainable by existing PIV techniques.

The calibration process for any imaging system is pivotal for relating the size of objects in an image to the actual physical dimensions. For the particle image velocimetry systems detailed above, the calibration process involves imaging a grid of points with a known spacing between each grid point. The spacing between the calibration points on the image can be

related back to the known spacing to provide the magnification at the focal plane. For three-dimensional systems, this calibration target must either be repositioned along the various depths or be three-dimensional in nature, requiring complex mapping to appropriately relate each calibration point to the appropriate point on the image [2]. The magnification of the camera is then used to compute the image distance of the camera. If the image distance and the focal length of the camera lens are known, the depth of any particle within a field may be established. Since the plenoptic camera is inherently designed to trace back the depth of particles throughout a volume, the magnification is only needed at the nominal focal plane. For this reason, a simplified method may be used to determine the image distance from the magnification, requiring only a single object of known size. This simplified method has been tested with transmission electron microscopes, but a detailed analysis on the accuracy of the image distance has yet to be performed [17]. While a conventional camera requires some form of external calibration, the design of the plenoptic camera may also be beneficial for an internal calibration method to determine the image distance based on the camera geometry. For the plenoptic camera, a focal point calibration image is necessary, where the aperture of the lens is stopped down so that only the pixels beneath the focal points of each of the microlenses is illuminated. The location of these focal points relative to the positions of the microlenses could provide enough information to back out the image distance of the plenoptic camera based on simple geometry. This thesis seeks to present both unique methods for determining the relationship between the dimensions in the image space and the dimensions in the object space, one using the principle of magnification and the other using the focal point calibration image. Both methods will be compared with the known length of the image distance to establish the accuracy and robustness of each method across a wide range of image distances.

Chapter 2

The Light Field and Plenoptic Imaging

A commercial version of the plenoptic camera was first released in 2011 by Lytro Incorperated. Although the plenoptic camera is relatively new in the realm of general photography, the principles of light field imaging that led to the development of the plenoptic camera have been studied for more than a century.

2.1 History

In 1908, Lippman introduced the concept of integral photography, a method for estimating the depth of an object from a single image. He theorized that, by placing a thin layer of transparent bumps onto the front end of a strip of film, the depth of a point light source could be estimated [18]. A diagram of this proposed method is shown in Figure 2.1. This idea provided the starting point for the development for all light field photography [14]. The nature of light and the full definition of the light field, a function that defines the propagation of light, were detailed in the work of Adelson and Bergen in 1991 [19]. Adelson

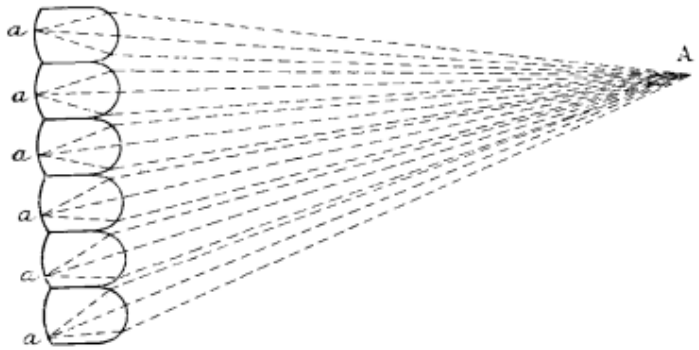

Figure 2.1: Lippmann's concept of integral photography [18].

and Wang then built upon this description in the following year with a proposed method for capturing the light field through the use of a single camera, which in design was similar to the concept originally supported by Lippman. This single camera system, named the plenoptic camera, included a lenticular array in front of the image sensor, as well as a field lens to properly focus the image onto each of the microlenses [20]. Gortler [21] and Levoy and Hanrahan [22] both presented the process by which a collection of light field data could be used to back out different focus points or perspectives of the viewed region from a single image. The work of Ng et.al. built upon the work of Adelson and Wang by making the plenoptic camera more accessible for general photography. By removing the field lens as a required component, the size of the plenoptic camera was reduced to dimensions comparable to a conventional camera, without sacrificing the four-dimensional capabilities. This work also combined the plenoptic camera with the principles of light field imaging developed by Levoy and Hanrahan [22] to demonstrate the multiple uses of the additional dimensions of the light field provided by the plenoptic camera [14].

2.2 Function of the Plenoptic Camera

The light field, as described by Adelson and Wang [20], is the function describing the complete distribution of light rays that are propagated within a free space. This field is parameterized by five dimensions: the spatial location (x, y, z) and the angle of propagation (θ, ϕ). Since light propagates in a straight line through a transparent medium, one of the spatial dimensions is redundant. For this reason, the plenoptic function is often reduced to a four-dimensional function, defined by $L_F(x, y, \theta, \phi)$. An image of a point source of light recorded by any camera captures the irradiance along the range of angles of light that pass through the aperture of the camera. If the magnitude of the range of angles that enter the camera is known, the depth of the point source of the light can be determined. While many forms of light field imaging utilize multiple cameras to capture the additional angular

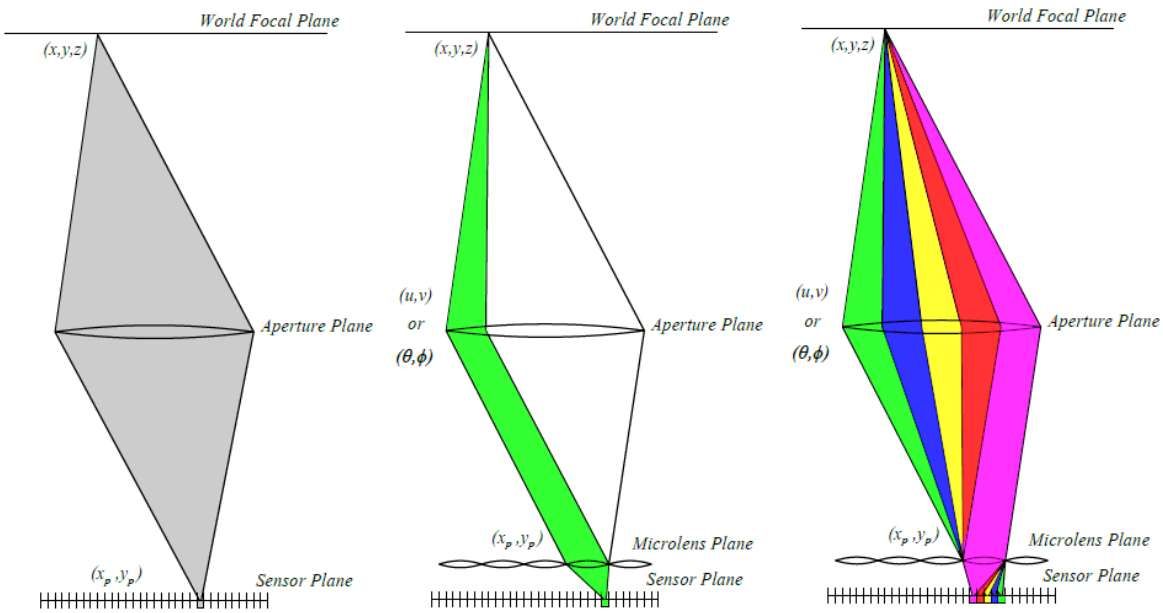

(a) Conventional camera (b) Single pixel's line of sight (c) All pixels' line of sight

Figure 2.2: Difference between a conventional camera and a plenoptic camera.

dimension, the plenoptic camera seeks to record the full light field onto just a single image sensor.

Conventional digital photography captures an image by recording the average intensity of the light that impacts a pixel, regardless of the angle of incidence. This can be seen in Figure 2.2(a). Light is emitted in every direction from the point source (x, y, z) located at the world focal plane. The portion of this light that is directed through the lens of the camera, highlighted in gray, is focused onto the single pixel located at (x_p, y_p), a spatial location. Therefore, the number of pixels on the image sensor of a conventional camera corresponds to the spatial resolution of the camera. The plenoptic camera follows the same imaging principles as a conventional camera, except that the point (x, y, z) on the world focal plane is mapped to a spatial location (x_p, y_p) on the microlens plane, rather than the sensor plane. Figure 2.2(b) shows the line of sight from the point (x, y, z) to a single pixel, highlighted in green. Unlike the conventional camera, the full distribution of light passing through the aperture of the camera is not focused onto a single pixel, but rather onto a single microlens. The light is then distributed across an array of pixels behind each microlens according to

Figure 2.3: A raw plenoptic image (3280 x 4904).

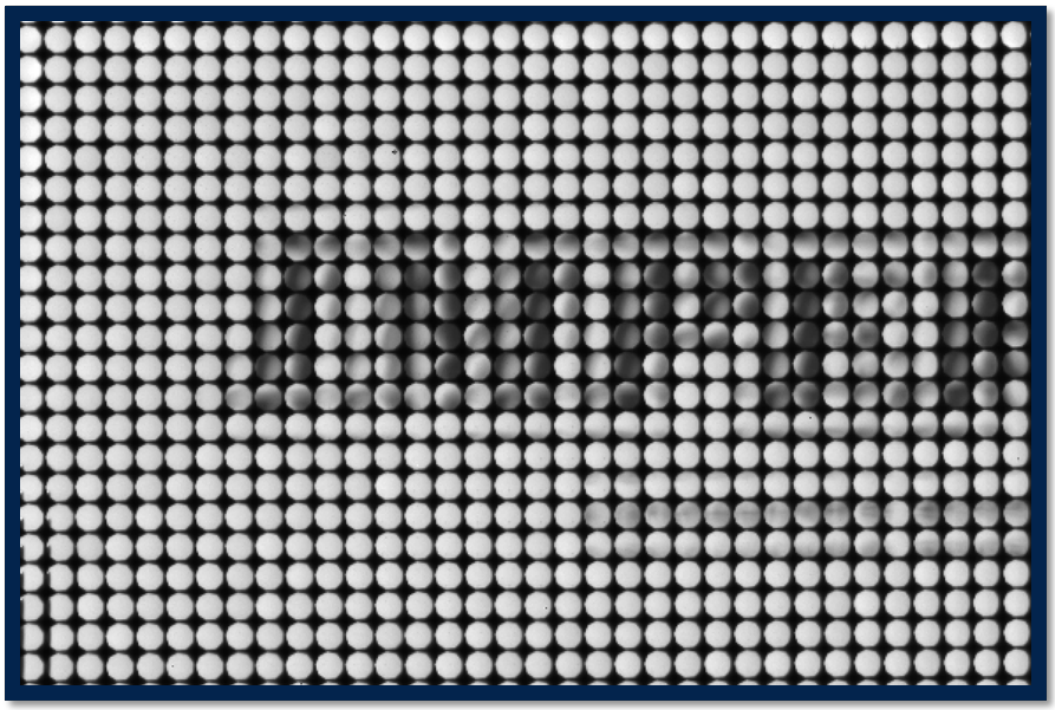

Figure 2.4: A portion of the plenoptic image.

the angle of incidence. Each pixel corresponds to a spatial location given by the position of the microlens, defined in the image as (x_p, y_p), but more commonly labeled as (s, t). In addition, each pixel also relates to the range of light rays passing through at a certain angle (θ, ϕ). This angular distribution can also be defined by the portion of the aperture through which the light rays propagate (u, v). Figure 2.2(c) expands on the previous figure to show the range of angles that correspond to each pixel for the given microlens [16].

There are inherent trade-offs associated with the plenoptic camera in order to retain the additional light field data. While the spatial resolution of the conventional camera is determined by the number of pixels on the image sensor, the spatial resolution of the plenoptic camera only corresponds to the number of microlenses contained within the array. This trade-off is an important consideration in the fabrication of the microlens array. Should there be too few microlenses, the reduced spatial resolution of the images would cause artifacts to appear in the rendered images. On the other end of the spectrum, too many microlenses would reduce the number of pixels that correlate to each microlens. Each microlens records a unique view of the light passing through the aperture, such that the grid of pixels beneath each microlens records the light passing through the full span of the aperture for that given spatial location. Since the circular aperture is imaged onto a square grid of pixels beneath each microlens, some pixels along the fringes of the associated grid are not illuminated. This can be seen in the raw plenoptic image in Figure 2.3, where the image appears to be comprised of individual circles. Figure 2.4 shows a closer look at a portion of this image, taken from the lettering on the Imperx box near the focal plane of the camera. The edge of each small aperture image is not perfectly round; rather, the edge is blurred around some of the neighboring pixels. These blurred pixels, as well as the dark portions, would affect the rendering of images requiring information near the edge of the aperture. Should the number of pixels beneath each microlens be too low, these partially illuminated pixels would overshadow the already limited number of fully defined pixels [23]. This proper balance depends on the properties of each plenoptic camera.

2.3 Perspective Shift and Refocus

The plenoptic camera is capable of two important post-rendering abilities: shifting the perspective from which the subject is viewed, and changing the location of the focal plane of the image. These abilities were first introduced by Levoy and Hanrahan [22] and later developed for the handheld plenoptic camera by Ng [14]. A perspective shift demonstrates practicality of relating each pixel to the portion of the aperture (u, v) through which the light passes, rather than the angle of propagation (θ, ϕ). A perspective image can be generated by selecting the pixel in each grid of a raw image, such as the one in Figure 2.3, that corresponds to the same portion of the aperture. This process is shown in Figure 2.5 [14]. Figure 2.6 shows four such perspective images, which correspond to light entering through four different points near the edge of the aperture. The individual images are labeled with respect to the portion of the aperture from which each perspective is viewed, as though looking out through the camera lens. Since each of these images is generated near the edge of the aperture, the effects of the dark pixels can be seen in the outer corners of each image. The curvature of the aperture can be clearly seen and partially impinges on each generated image. This perspective shift capability exhibits the range of parallax available to the plenoptic camera, comparable to results that would have previously required four conventional cameras.

Not only can desired objects be viewed from different perspectives, but the plenoptic camera is also capable of rendering images at various focal planes, still from the same raw image shown in Figure 2.3. From general imaging, the depth of the focal point of an image is based on the focal length of the lens and the distance from the lens to the imaging plane, which is the microlens plane for the plenoptic camera. Therefore, to change the depth of the focal point for a given lens, a synthetic microlens plane can be assumed to be at a different distance from the lens, as shown in Figure 2.7. This new location is represented as a scale factor multiplied by the actual location of the plane, labeled as α. To focus on objects in front of the nominal focal plane, the synthetic image plane must be further away from the lens, such that α must be greater than unity. Conversely, to focus on objects behind the nominal focal

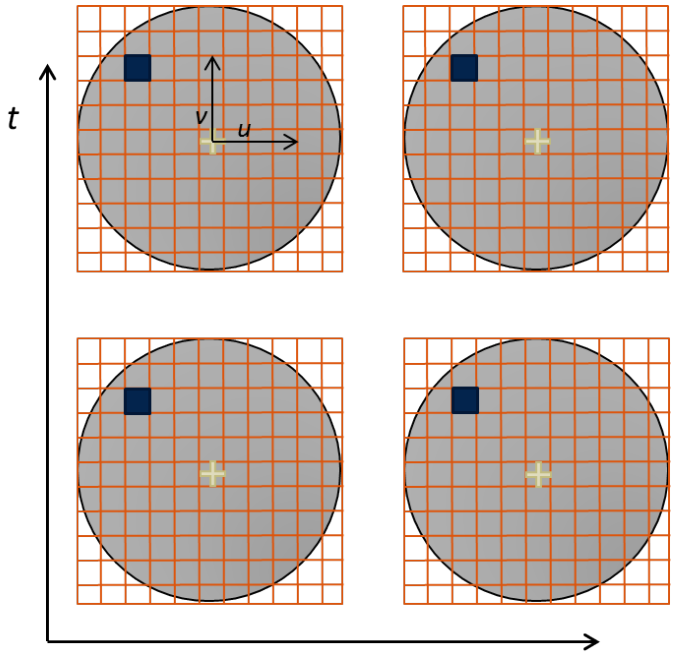

Figure 2.5: Perspective image generation by angle.

(a) Upper right

(b) Upper left

(c) Bottom right

(d) Bottom left

Figure 2.6: Different perspectives generated from Figure 2.3 (193 x 287).

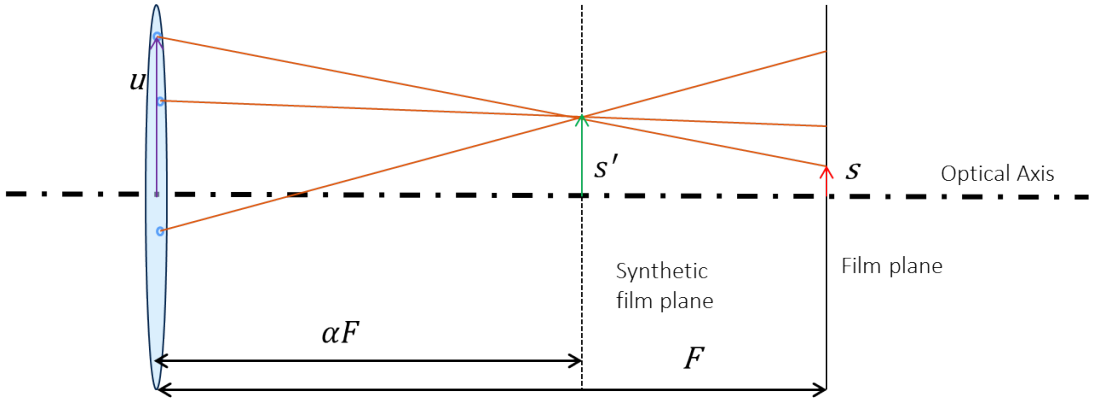

Figure 2.7: Geometry of a synthetically generated focal plane

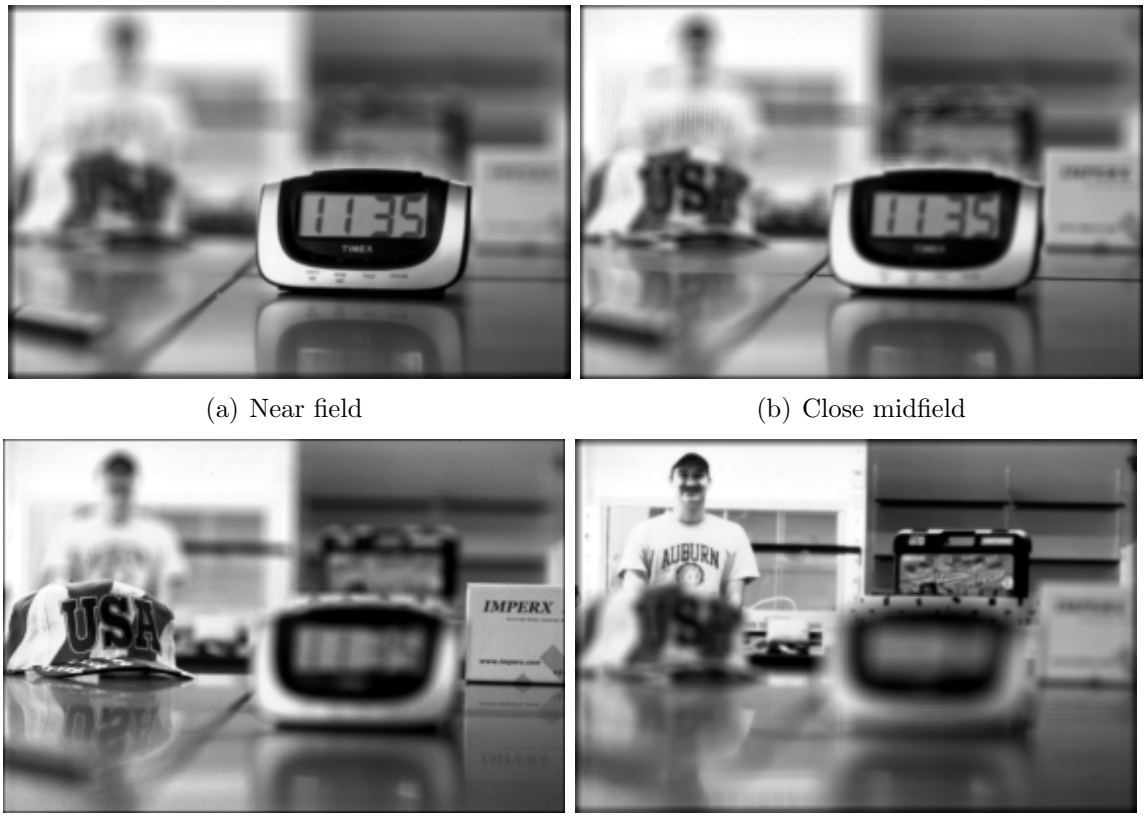

(a) Near field

(b) Close midfield

(c) Far midfield

(d) Far field

Figure 2.8: Different focal planes by synthetic plane (193 x 287)

plane, α must be less than unity. The pixels that correspond to each microlens are no longer directly beneath the microlens, but rather must be reestablished based on geometry. All the pixels for a given microlens are then averaged to provide the intensity for that microlens [14]. Figure 2.7 shows the image of the room refocused at different depths. One important distinction with the plenoptic camera from other imaging systems is that each object does not have to be in focus in the original plenoptic image in order for the object to be in focus in a rendered image. For example, the clock in the foreground of Figure 2.3 is clearly blurred, but this clock is in clear focus in Figure 2.8(a). While current PIV techniques require that all particles be in focus to be reconstructed, the plenoptic camera would be able to reconstruct particles throughout a thicker depth.

2.4 Further Developments

Since the fundamentals of the handheld plenoptic camera were developed in 2005, many have sought to improve on the capabilities of the camera. For the plenoptic camera develeped by Ng et.al. [14], the spatial resolution of a reconstructed image is limited by the number of microlenses. Lumsdaine and Georgiev [24] proposed a different configuration for a plenoptic camera that would allow for images to be generated with higher resolution. Figure 2.9 shows the difference between the camera developed by Ng et.al. [14], which Lumsdaine

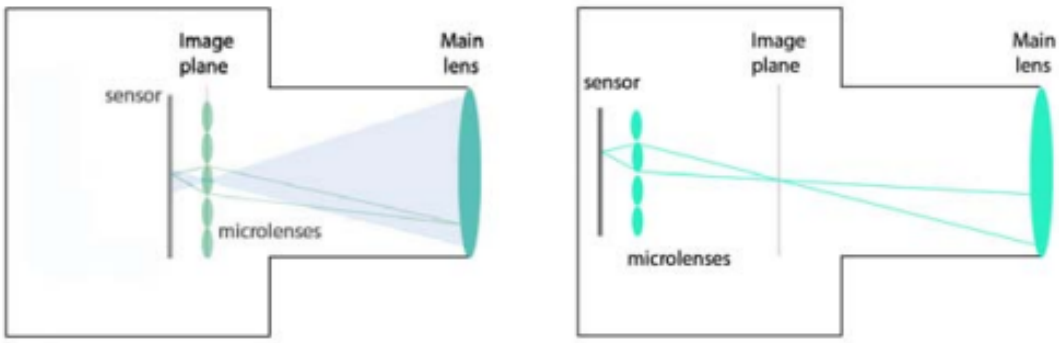

(a) Plenoptic 1.0 (b) Plenoptic 2.0

Figure 2.9: Comparison between plenoptic 1.0 and plenoptic 2.0 [24].

and Georgiev [24] referred to as plenoptic 1.0, and the new model, called plenoptic 2.0. For plenoptic 1.0, the main lens is optimally focused onto the microlens plane, such that each microlens records an image of the full aperture. In contrast, plenoptic 2.0 is optimally focused well in front of the microlens array, so that each microlens only records a portion of the aperture. This camera arrangement allows the camera to fully utilize the positional information of the light entering the camera to render images in full resolution, as named by Lumsdaine and Georgiev [24]. A comparison of the difference between a plenoptic 1.0 rendered image and a plenoptic 2.0 rendered image is shown in Figure 2.10. The plenoptic 1.0 image has several artifacts due to the strong contrast of colors in the image and the limited spatial resolution. The full resolution image significantly reduces these artifacts and allows the fence on the right of the image to be distinguished from the many colors of the bush. Plenoptic 2.0 has become the leading form of plenoptic imaging in the commercial industry [24]. While the plenoptic 2.0 provides superior resolution in generated images, the additional resolution is at a cost to angular resolution. For this reason, plenoptic 1.0 is better suited for plenoptic PIV, and shall be the focus for the rest of the paper.

Figure 2.10: A light field image, a normally rendered image, and a full resolution image [24].

While the alignment and capture of a volume of particles is simple to execute with a plenoptic camera, especially in comparison with other three-dimensional PIV techniques, the processing of the plenoptic images to determine the velocity field has proven to be the main challenge. Lynch [25] proposed that a window displacement iterative multigrid (WIDIM) method, originally published by Scarano [26], could be used to determine the velocity field

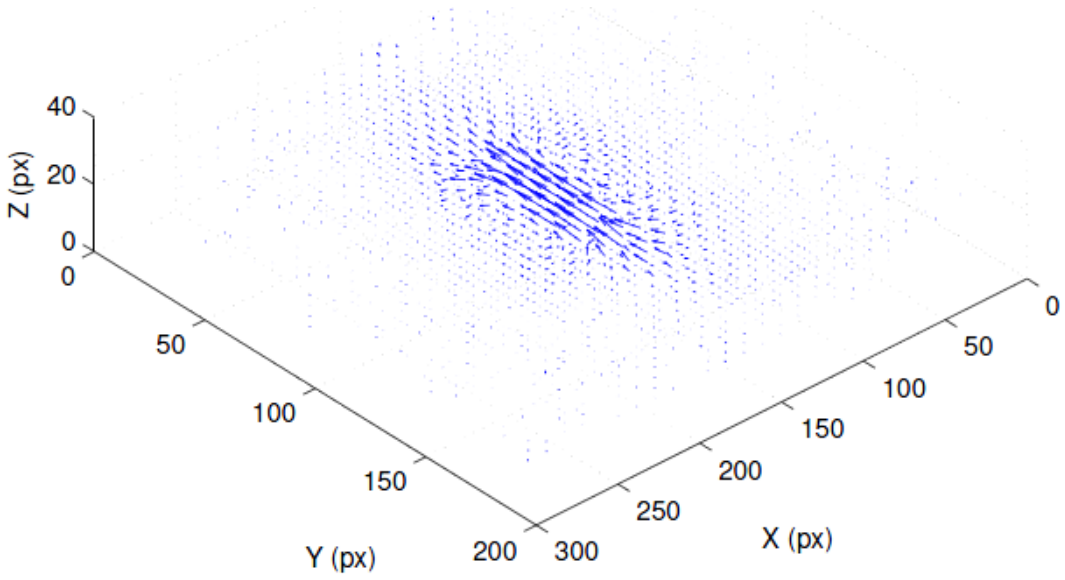

Figure 2.11: Velocity field of an inviscid spherical vortex [25].

from a plenoptic image. Lynch [25] extended this algorithm into a three-dimensional method by applying this analysis to multiple rendered focus planes. One such case was the Hill's spherical vortex, shown in Figure 2.11. The reconstructed flow field proved to match the velocity characteristics expected with an inviscid vortical flow. Despite the proven accuracy, rendering the focal planes to determine the location of the particles within the flow still has significant drawbacks. For example, this method may only be used with a low particle number density. This restriction may only be overcome through the use of more advanced reconstruction methods.

Current progress is being done by Lynch [15] and Fahringer [16, 27] to develop a tomographic method for reconstructing a particle field from a plenoptic image. The process of volumetric reconstruction using computed tomography algorithms has been used for several decades. In 2006, Elsinga et.al. [7] introduced the concept into the field of fluid diagnostics as a method for obtaining three-dimensional velocimetry data, termed tomo-PIV. Prior to the reconstruction process, the volume of interest is discretized into cubic voxel elements, which are the volume equivalent of pixels. For tomo-PIV, these elements are the size of a pixel; however, for a plenoptic camera the size of the voxels is chosen to reflect the size

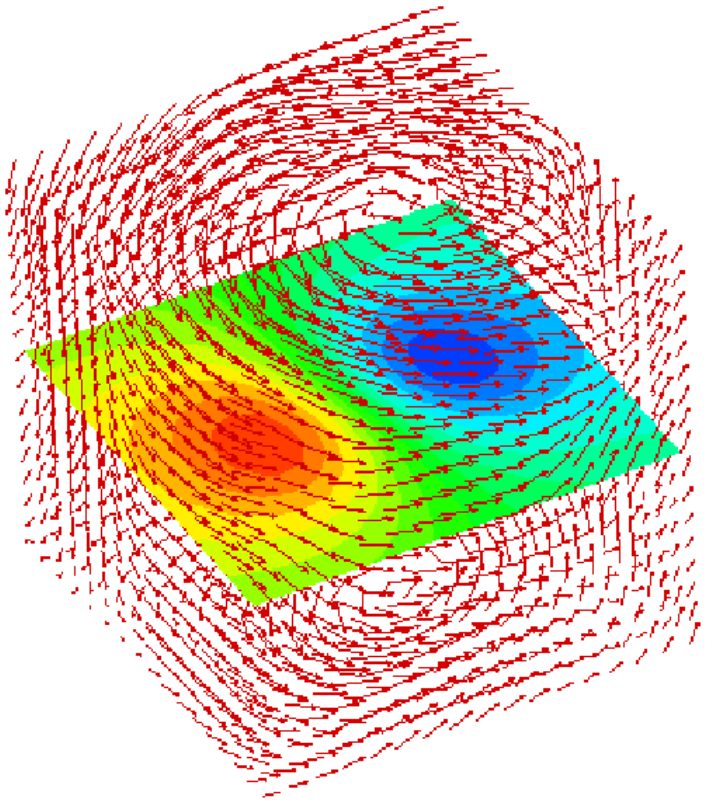

Figure 2.12: Velocity field of a synthetically generated vortical particle displacement [15].

of a microlens, since the microlenses govern the spatial resolution of the plenoptic camera. Tomographic algorithms then seek to map the intensity recorded by each pixel on the image sensor to each voxel in the three-dimensional volume. This mapping is of critical importance for a proper reconstruction and is dependent on an accurate estimation of the distance between the main lens and the microlens array of the plenoptic camera. Although plenoptic PIV simplifies the imaging system to one camera, the reconstruction algorithm remains computationally intensive. In many other PIV methods, each image pair is cross-correlated to determine the direction of movement for a group of particles. In tomographic PIV, however, each time step is reconstructed first, and then the two reconstructed particle fields are cross-correlated.

With the tomographic approach for determining the velocity field, much higher particle seeding may be used. Similar to the focal stack algorithm developed by Lynch [15], this

method was tested with a synthetic vortical flow, though this time an Oseen vortex was used. The resulting velocity field produced by the tomographic algorithm applied to a plenoptic image is pictured in Figure 2.12. This preliminary test showed that plenoptic PIV was capable of quantifying the velocity within the main motion of this vortex, but with apparent distortion in the depth direction. This depth distortion was also apparent in the work of Fahringer and Thurow [27], where reconstructed particles were elongated in the depth direction. This is attributed to the limited parallax of the plenoptic camera, which is restricted by the small size of the camera. The centroid of these particles was found to still be located at the expected depths, demonstrating that this elongation does not dramatically undermine the feasibility of plenoptic PIV.

2.5 Assembly of the Plenoptic Camera

The camera used in the two main plenoptic camera experiments in Section 2.4 was modeled after the design detailed in Ng et.al. [14]. The image sensor used by this camera is a Kodak KAI-16000 charge-coupled device (CCD), which has a pixel size of 7.4 μm. The microlens array was fabricated from a 10.4 mm thick glass slab to form 193 x 287 microlenses,

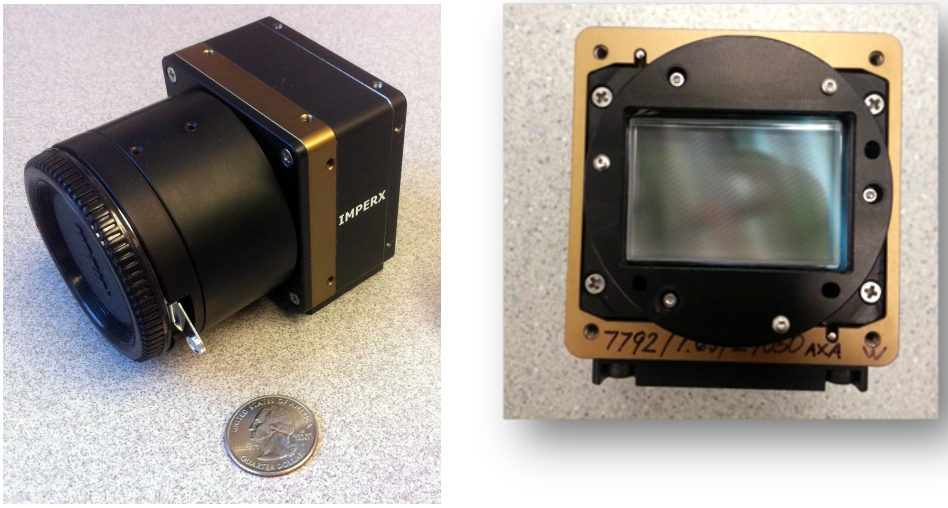

(a) Plenoptic camera (b) Microlens mount

Figure 2.13: Properties of the Auburn University plenoptic camera.

which in turn is the spatial resolution for this plenoptic camera. Each microlens has a pitch of 125 μm, with a manufacturer-specified non-cummulative error of ±3%. Since the resolution of the image sensor is 3280 x 4904 pixels, the light through each microlens is divided among a grid of approximately 16 x 16 pixels, representing 256 unique angles of incidence for each spatial location. Despite its ability to capture the full light field, the plenoptic camera is no larger than a conventional camera. This can be seen in Figure 2.13(a), where the plenoptic camera is compared with the size of a quarter.

Figure 2.14: The process of aligning the microlens array.

The microlens array in a plenoptic camera is ideally placed in front of the image sensor at a distance equivalent to the focal length of the microlenses, which is 500 μm for the camera in Figure 2.13(a). A mount for the microlens array is designed to be able to change the alignment of the microlens array through tightening or loosening of the three inset screws on the circle plate seen in Figure 2.13(b). To determine if the array is properly focused after the array is placed into the camera, the lens is removed and collimated light is shined through the array and onto the image sensor. The plenoptic camera shown in Figure 2.14 exhibits the characteristics of a properly aligned array. The collimated light is equivalent to a point source at optical infinity, and so the resulting image should show that the light passing through each microlens is focused onto a single pixel across the entire array. Since the point of focus can only be estimated to within the span of the pixel, there is some potential for error in

the distance of the array from the image sensor, although slight. For the plenoptic camera used with this work, the pixel pitch of 7.4 µm signifies that any placement within ± 25 µm of the nominal placement depth will appear to be in focus. The screws are adjusted until every microlens is properly focused. This process must be repeated any time the microlens is removed or cleaned to ensure that no artifacts are caused by improper alignment. This alignment step is important for angular clarity, as a misalignment would cause the intensity for a given angle to be blurred across several pixels.

Chapter 3

Estimating Image Distance

The image distance S_i, defined as the length from the main lens to the microlens array, is pivotal in relating the size of objects in an image to the physical dimensions of the object. The tomographic reconstruction process for plenoptic PIV heavily depends on this parameter to calculate the mapping between each pixel and voxel element. Unfortunately, this property is a dimension inside of the camera and therefore cannot be directly measured.

3.1 Current Calibration Method

Although the magnification method of calibration has yet to be fully analyzed for accuracy, this method has been used in recent plenoptic PIV experiments with reliable results [15, 27, 16]. The magnification method requires two calibration images to be taken: one of a white sheet to determine the location of the focal points of the microlenses and another of a ruler to determine the magnification of the current lens arrangement.

3.1.1 Focal Point Calibration Image

In the two-plane parameterization of the light field, each light ray is represented by the points of intersection with each plane: the main lens aperture plane (u, v) and the microlens plane (s, t). Whenever the focal settings of the camera are changed, the camera must be calibrated to relate the light ray that a pixel records to the corresponding intersection of that ray with the microlens array and the aperture of the camera. These intersections must be determined through consideration of the geometric relationship between the image sensor plane, or the pixel coordinates (x, y), and the aperture plane (u, v). This relationship is shown schematically in Figure 3.1, where similar triangles can be used to relate the image

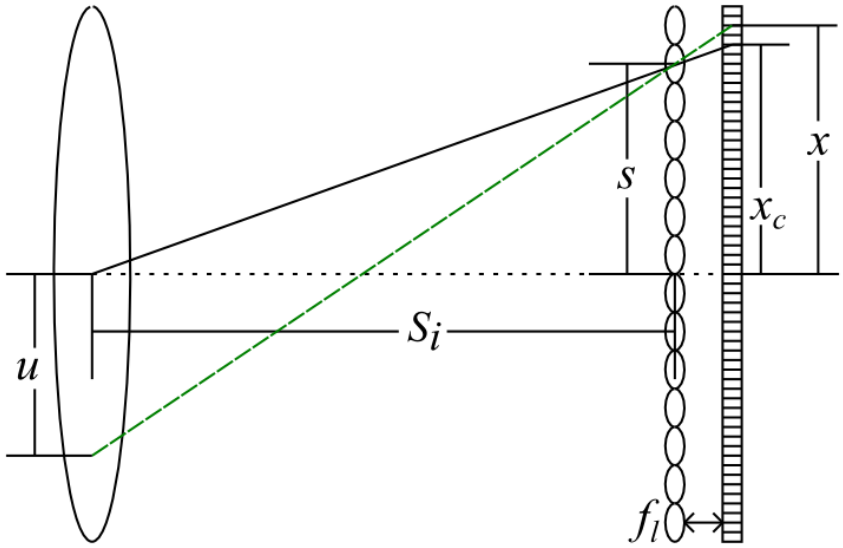

Figure 3.1: Relationship between aperture and pixels.

coordinates to aperture coordinates. In order to quantify this relationship, the image distance S_i and the center of the aperture image under each microlens x_c must be determined. The determination of the image distance S_i is the purpose of this paper and will be thoroughly detailed later. To determine the center of the aperture in each microlens image x_c, a simple calibration step is performed by reducing the aperture of the main lens to the minimum value. The reduced aperture only allows light to pass through the center of the main lens, and only the pixels corresponding to the centers of each aperture subimage will be illuminated under each microlens. A subset of a calibration image is shown in Figure 3.2(a). The number of bright spots corresponds to the number of microlenses, and the centroid of each of the spots corresponds to the center of the aperture subimages. Since the intensity might be spread across a few surrounding pixels, the location of the exact centers can be found with sub-pixel accuracy by using a simple centroid fit. The locations found by the centroid fit are represented by a green "x" in Figure 3.2(b) [27].

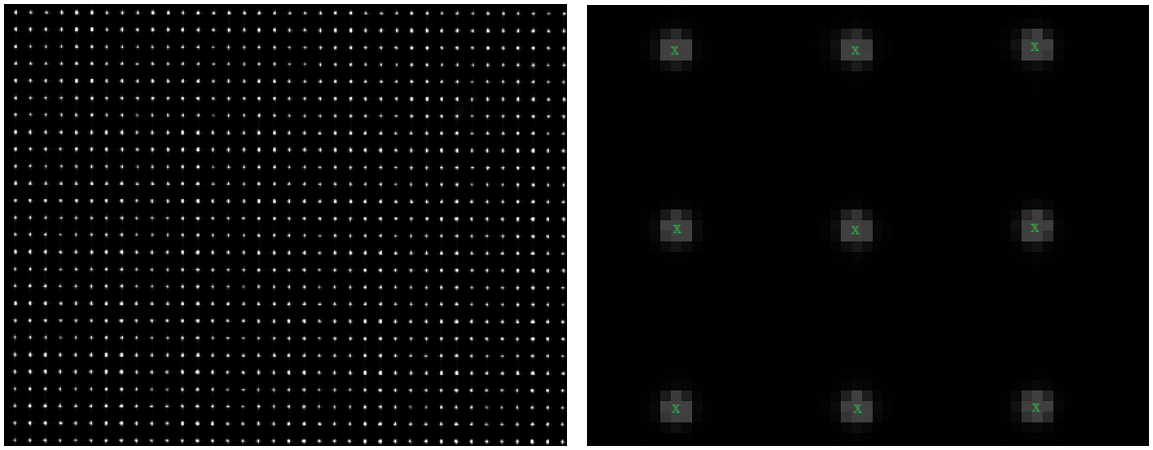

(a) Subset of the calibration image (b) Centroid fit for subpixel accuracy

Figure 3.2: Calibration image.

3.1.2 Image Distance by Magnification

While the values of x, x_c, and f_m can be determined based on the geometry and the propagation of light within the camera, the magnification method of determining the image distance S_i requires an object external to the camera to be used for calibration. To relate distances inside the camera to distances outside of the camera, the coordinate system is defined by the optical axis, as shown by the dotted line in Figure 3.3, and the main lens. The origin is located at the intersection of these two planes, at the center of the main lens. All points to the left of the origin, outside of the camera, are defined as the object space, denoted by a subscript o. To the right of the origin is the interior of the camera, known

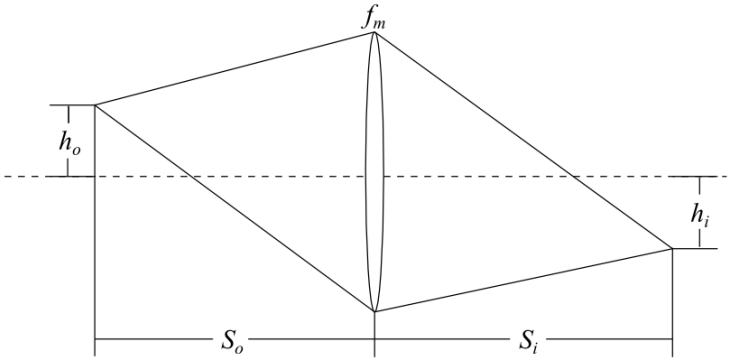

Figure 3.3: Distances in the object and image spaces.

as the image space and denoted by a subscript i. In a two-dimensional system, such as in Figure 3.3, the distance from the optical axis is expressed as the height h, while the distance from the main lens is the depth S. The microlens array is located at a distance S_i from the main lens, although not shown in the figure for simplicity.

Based on geometric optics, there are two principle equations to relate the object space to the image space: the thin lens equation and the magnification equation. The thin lens equation, defined as

$$\frac{1}{S_o} + \frac{1}{S_i} = \frac{1}{f_m} \tag{3.1}$$

relates the depths of the plane on either side of the camera to the focal length of the main lens f_m. Similarly, the magnification equation, expressed as

$$M = -\frac{h_i}{h_o} = -\frac{S_i}{S_o} \tag{3.2}$$

relates the ratio of the depths to the ratio of the heights, based on similar triangles. If the magnification and focal length of the main lens are known, the depths of the focal planes can be easily determined by rearranging Eqs. (3.1) and (3.2) to produce

$$S_o = \frac{f_m\,(M-1)}{M} \tag{3.3}$$

$$S_i = f_m\,(1-M) \tag{3.4}$$

While the focal length of the main lens is a set value, the magnification of the lens depends on variable properties of the lens, such as the focal settings. In order to determine the magnification for a lens with fixed characteristics, an object of known dimensions may be imaged. An ideal object for this method is a ruler, as shown in Figure 3.4. To determine the magnification, a span of visible centimeters is chosen, such as the range from 29 cm

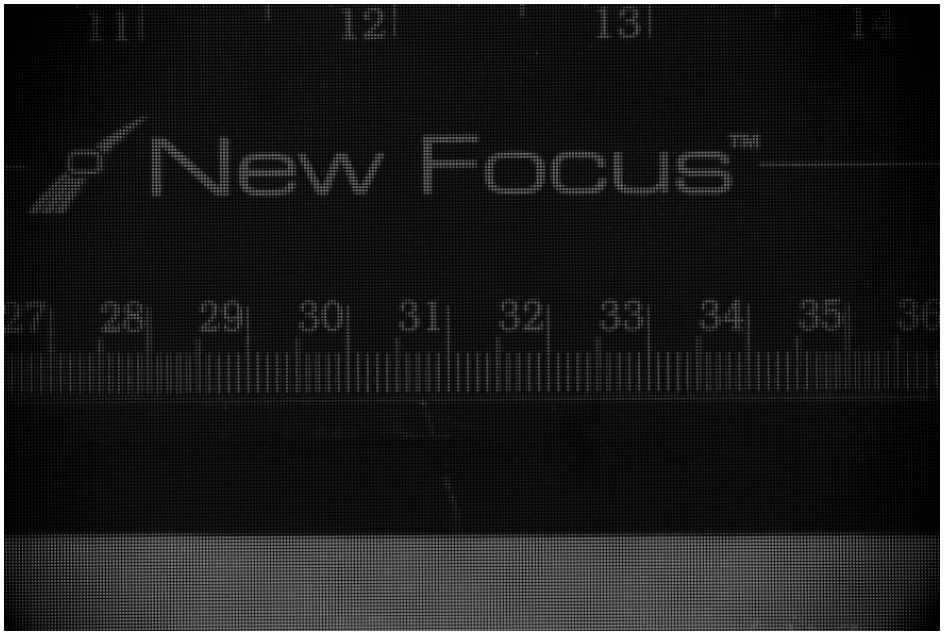

Figure 3.4: Ruler calibration image.

to 33 cm in Figure 3.4. Between these two points on the image, there are 155 individual microlenses, which correspond to an image distance d_i of approximately 19.3 mm based on the pitch of the microlenses. The magnification can be deduced by dividing this distance by the actual distance d_o between these two points, which produces a magnification of -0.39. Since Figure 3.4 was taken with a 135 mm lens, the value for the image distance S_i can be approximated using Eq. (3.4) to give an expected value of 185 mm. Notably, the accuracy of this method is constrained by the width of the microlenses, although better detail may be attained by interpolating between the microlenses to find the proper location of the ruler marking.

One predicted problem with this method is the inaccuracy caused by the depth of focus. The depth of the focus is the region surrounding the focal plane in the object space where an object will appear to be in focus. The size of this region is dependent on three camera parameters: the object plane distance S_o, determined by Eq. (3.3); the magnification of the camera M, determined by Eq. (3.2); and the diameter of the main lens d, given by the $f/\#$

of the lens [28]. The front distance L_1 and back distance L_2 of the depth of focus can be determined from

$$L_1 = \frac{CS_o}{d + C} \tag{3.5}$$

$$L_2 = \frac{CS_o}{d - C} \tag{3.6}$$

where C is the circle of confusion. This is the uncertainty caused by the spatial resolution of the camera, and the value is given by

$$C = p_m/M \tag{3.7}$$

where p_m is the size of a microlens. From these equations, the total span of the depth of field can be written as

$$\Delta S_o = \frac{C^2 S_o}{d^2 + C^2} \tag{3.8}$$

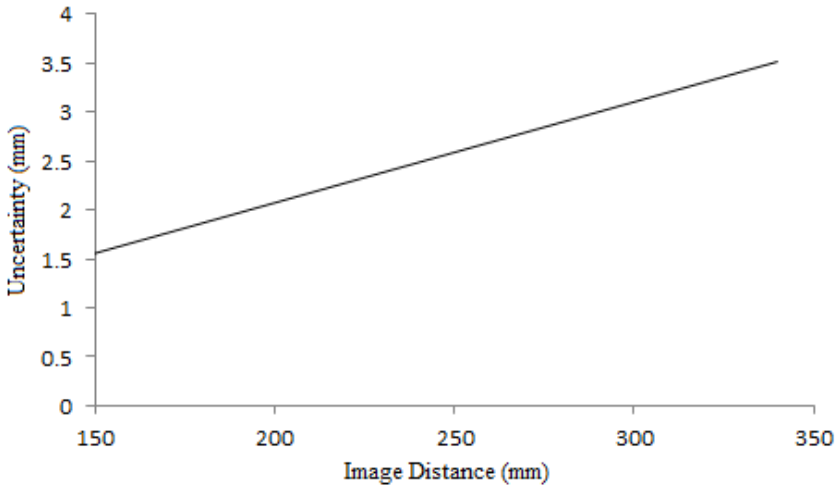

Figure 3.5: Uncertainty with respect to image distance for a 135 mm lens.

This can easily be equated to a change in S_i by taking the derivatives of Eqs. (3.3) and (3.4) with respect to the magnification and combining them into a single equation, such that

$$\Delta S_i = M^2 \Delta S_o \tag{3.9}$$

Figure 3.5 shows the relationship between the image depth to the region of uncertainty in the prediction of this value caused by the range of the depth of focus. This uncertainty is applicable for a main lens with an a focal length of 135 mm and an $f/\#$ of 5.6. For many PIV experiments, the image distance is high in order to bring the focal plane closer to the camera to reduce the width and height of the illuminated volume. As the image distance is increased, the uncertainty in the approximation of the image distance linearly increases, such that the uncertainty is roughly equal to 1% of the image distance. Thus, an error of this magnitude should have a minimal effect on the reconstruction of a volume.

Another possible source of uncertainty with the magnification method for determining the image distance is a miscalculation in the height of an object in the image plane. The spatial resolution of the plenoptic camera is limited by the number of microlenses, and so the measured value of the image height may be improperly estimated. The relationship between the error in the image distance to the error in the estimated height of an image is given by

$$\frac{\Delta S_i}{\Delta d_i} = \frac{f_m}{d_o} \tag{3.10}$$

For an extreme case, if only a one centimeter span of a ruler is used to provide the object height for a 135 mm lens and the image height was offset by the entire width of a microlens with $p_m = 125$ μm, the resulting error in the approximation of the image distance would only be 1.69 mm for all values of the image distance. As stated, this is only an extreme case, and the error can be greatly reduced by using a larger span along the ruler and using an interpolation method to determine the precise image distance. Therefore, the main source of error for the magnification method is the depth of focus. Overall, the magnitude of the

uncertainty is expected to be low for the magnification method of determining the image distance.

3.2 Estimating S_i from Location of Microlens Centers

With the inclusion of a microlens array inside of the camera, the plenoptic camera offers the possibility of determining the magnitude of the image distance based on the focal point calibration image rather than through magnification. Since the spacing between each microlens is approximately 125 μm, the image distance could be approximated by examining the spacing between each aperture subimage. The spacing is relatively large when the image distance is small, but the average spacing decreases as the lens is moved further away from the sensor. By establishing a relationship between the spacing in the focal centers to the spacing in the microlenses, the precise image distance could be established. This alternative calibration technique would not require the additional ruler image to be taken for each experiment and only need the single focal center calibration image to be taken. For the focal point calibration image, a white sheet is placed directly in front of the lens regardless of the focal plane. Thus, unlike the magnification method of calibration, access to the focal plane of the experimental arrangement would not be necessary.

3.2.1 Model of Relationship

Since there are two principle planes, the microlens plane and the image plane, the origin of the coordinate system could be positioned on either plane. The image sensor is at a fixed position and orientation, and the microlens array should be positioned 500 μm in front of the image sensor for the camera described in Section 2.5. There is potential for error in this placement, however, as the array may not be centered on the optical axis, or may not be perfectly focused onto the image sensor. For this reason, the distance between the microlens array and the image sensor is labeled by $\overline{f}$ to denote the potential flexibility of this position. The origin of the coordinate system, defined as (s, t, z), should therefore be placed at the

center of the image sensor, as shown in Figure 3.6, since this point is consistent regardless of any changes to the camera. The optical axis is defined by a line perpendicular to the image sensor, originating from the center point of the sensor. The location of the center of a microlens in the array with respect to the optical axis is then defined by the vector $\vec{d}$. This vector can be split into the three components (d_s, d_t, d_z), where $d_z = \overline{f}$. Similarly, the location of the focal center on the image sensor is labeled by the vector $\vec{p}$, and can be divided into the components (p_s, p_t).

3.2.2 Algorithm Development

Before the relationship between the focal points and the image distance can be established, the precise location of each of the microlenses must be determined with respect to the (s, t) plane shown in Figure 3.6, where the t axis is orientated out of the paper. During the initial placement of the microlens array, through the process described in Section 2.5, an image is taken after the full array has been properly aligned. Since the collimated light entering the camera should be perfectly perpendicular to each microlens, the focal point of each lens will lie on the pixel directly beneath the center of that microlens. Thus the location of each microlens on the (s, t) plane is equivalent to the location of the illuminated pixel on the image sensor.

From here, an algorithm is developed to take the position of the microlens array and the location of the centers, which are determined from the focal point calibration image, to back out the proper value of S_i. The relationship between a point on a microlens array and a point on the image sensor is modeled using the simple geometry of similar triangles, as can be seen in Figure 3.6. The resulting relationship equation can be expressed as

$$p_{s,\text{est}} = \left(\frac{S_i + \overline{f}}{S_i} \right) d_s \tag{3.11}$$

This equation is shown in the (s, z) plane, but the same relationship exists for the (t, z) plane as well. Based on this equation, only one data point would be needed to back out the

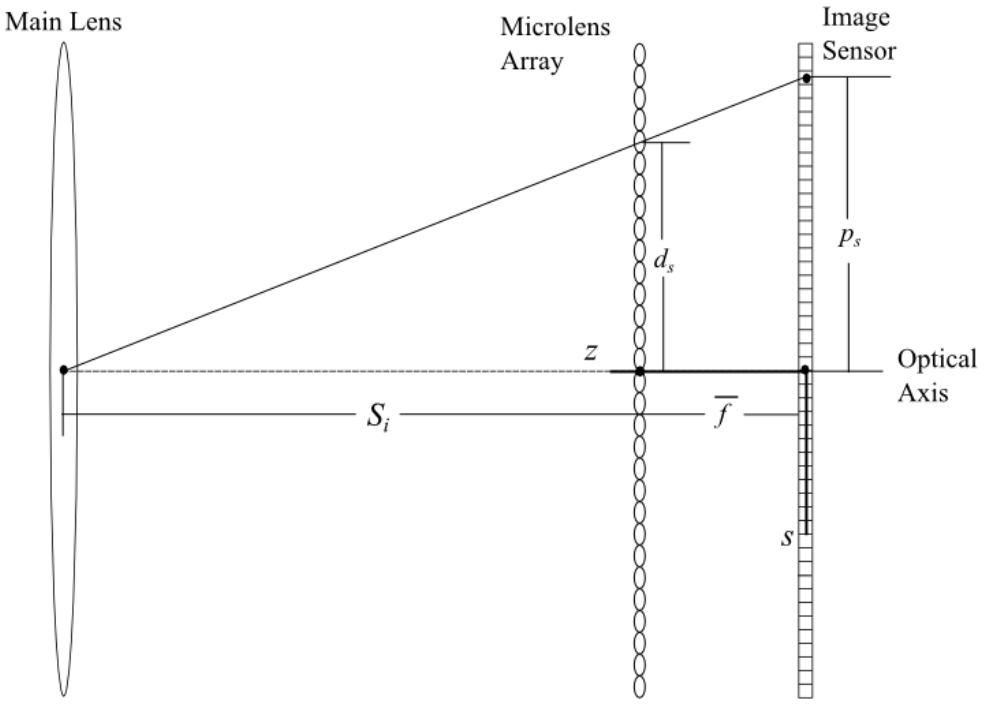

Figure 3.6: coordinate system and geometry of internal parameters.

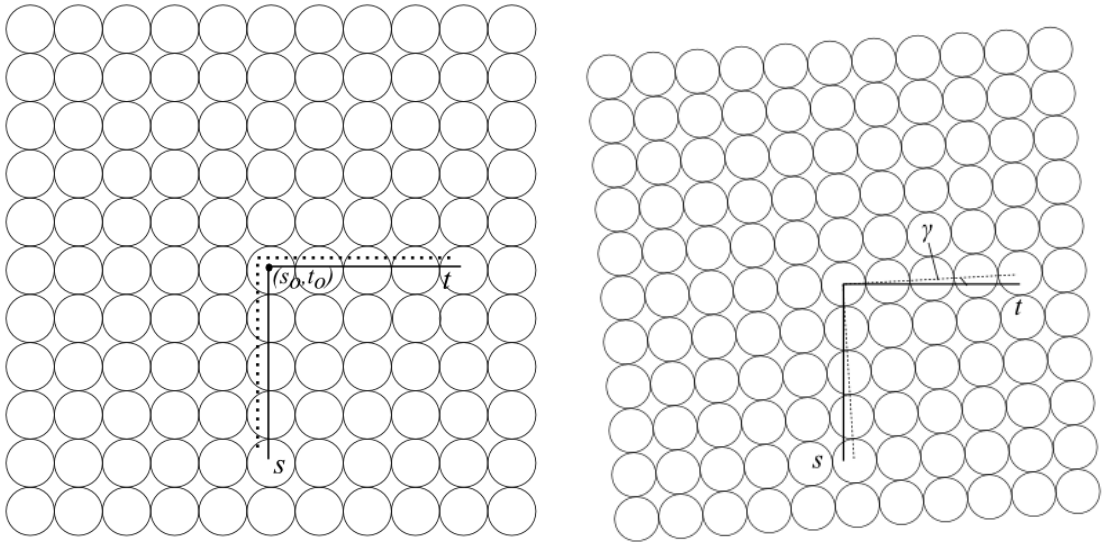

(a) Shift

(b) Rotation

Figure 3.7: Imperfections to microlens array placement.

image distance that would satisfy this relationship. To fully utilize each of the points and best estimate the value of S_i that properly represents a given geometry, a value is assigned to S_i, and the known microlens positions are used to calculate where the focal points of the microlenses would be for the given value of S_i. These new focal locations are then compared with the location of the centers that are input into the program until the root mean square error is minimized, defined by

$$e_{\text{RMS}} = \sqrt{\frac{\sum_{i=1}^{m}\sum_{j=1}^{n}[(p_s(i,j) - p_{s,\text{est}}(i,j))^2 + (p_t(i,j) - p_{t,\text{est}}(i,j))^2]}{2mn}} \tag{3.12}$$

where m and n are the dimensions of the microlens array. The value for S_i is then altered using the built-in MATLAB function $fminsearch$ until the root mean square error is minimized.

Although the process for obtaining the microlens position is sound, there is possible error if the light source for the microlens alignment image is not far enough away from the lens. For the plenoptic camera used in this experiment, the microlens array of the camera was known to be off-centered from the optical axis, as well as slanted to the left. The magnitude of these errors is defined by two spatial variables (s_o, t_o) and one rotational variable γ, which are geometrically depicted in Figure 3.7. Ideally, the alignment image should compensate for these positional errors. These errors are applied to the (s,t) locations given by the alignment image through the equations

$$d_{s,\text{new}} = (d_{s,\text{old}} + s_o)\, cos(\gamma) - (d_{t,\text{old}} + t_o)\, sin(\gamma) \tag{3.13}$$

$$d_{t,\text{new}} = (d_{s,\text{old}} + s_o)\, sin(\gamma) + (d_{t,\text{old}} + t_o)\, cos(\gamma) \tag{3.14}$$

Instead of simply iterating for the image distance, the magnitudes of the misplacement parameters are iterated until the best fit is achieved. For a proper microlens alignment

process, all three of these values should be negligible. Any other result would require another method for ascertaining the precise location of the microlens centers to be generated.

3.2.3 Synthetic Design

Fahringer and Thurow [16] have developed a program called the Auburn Light Field Analyzer (ALFA) that is capable of simulating focal point calibration images. These calibration images are generated by simulating several thousand particles in front of the camera to be equivalent to the light source provided by a white background. The properties of the camera are then specified in the program, and ray transfer matricies are used to map the thousands of rays emanating from each particle to the point of intersection with the microlens array and then onto the image sensor. For each synthetic image, the microlenses are properly aligned with the image sensor, separated precisely by the focal length of the microlenses, or 500 μm in this case. For all synthetic experiments, the simulated plenoptic camera has properties that match the camera detailed in Section 2.5, with an image sensor size of 3280 x 4904 pixels with a pitch of 7.4 μm. The microlenses are spaced evenly at a pitch of 125 μm with an array size of 193 x 287 microlenses. The focal length of the lens was chosen to match a lens currently owned by the lab to best match experimental testing, and was set to 135 mm. Rather than input the value for S_i, ALFA requires the magnification of the lens. The magnification was varied from a value near 0 to 2 in increments of $0.\overline{33}$, which corresponds to image distances ranging from 135 mm to 405 mm. The centroid method was then used on the resulting images to determine the location of the focal points, as detailed in Section 3.1.1. From here, each set of focal points, as well as the perfect microlens array, were passed into the algorithm described in the previous section to test the accuracy of the image distance prediction.

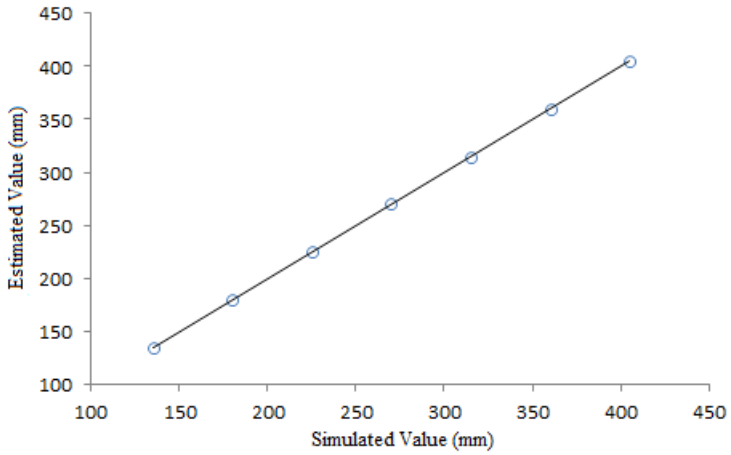

Figure 3.8: Synthetic results for image distance prediction.

3.2.4 Synthetic Results

Figure 3.8 shows the results of the estimation of the image distance for each of the generated images, where the black line represents the ideal solution. It can be clearly seen that the synthetic results show a robust and accurate prediction for S_i for every simulated value. Each estimated value falls within 0.05 mm of the actual value, thus demonstrating an accuracy that outperforms the ruler magnification method. Also, all values for the error parameters remain less than 10^{-6}, hence demonstrating an ideal placement of the microlenses. These results showed that the basic premise behind this method for estimating the image

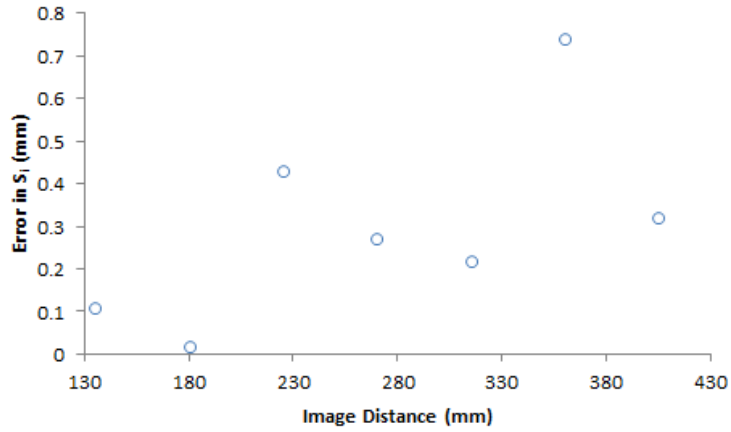

Figure 3.9: Error caused by a random noise of ± 1 pixel for a 135 mm lens.

distance is sound. To further test the robustness of the algorithm, a random noise was applied to each of the focal center locations. The uncertainty in location was varied up to a full pixel width of ±7.4 μm in order to simulate the effect of either an improperly spaced microlens or the known window of error for the centroid fit to find the focal points. Even with a noise error of a full pixel, all of the estimated image distance values are found within 1 mm, as seen in Figure 3.9.

3.2.5 Preliminary Experimental Results

A Nikkor 135 mm lens was used to test the practicality of this focal point calibration method. In order to vary the image distance, extension tubes were added to the lens, and the known image distance was assumed to be the the image distance at optical infinity, which was 135 mm for this lens, plus the total length of the extension tubes. The microlens array was assumed to have a perfect pitch of 125 μm between each microlens. The displacement parameters s_o, t_o, and γ were all outputs for the algorithm, and the magnitude of the rotation parameter γ was confirmed to be correct by calculating the angle of rotation between two focal points located on the same row of the microlens array. Since the algorithm properly estimated this value, the magnitudes of the two displacement terms should also be accurate.

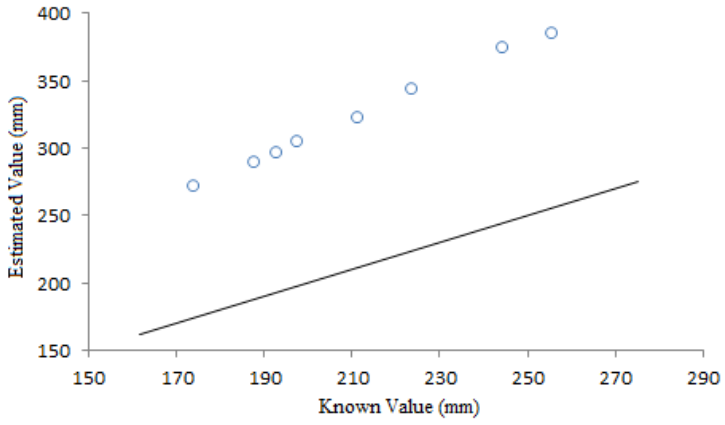

Figure 3.10: Experimental results for image distance prediction.

For the experimental results displayed in Figure 3.10, the value of the calculated image distance drastically differed from the known image distance. The large difference between the expected result and the actual result demonstrates that this problem cannot be attributed to a noise error and that there is a significant flaw in the model of the camera. This reasoning is further supported by the uniformity of the observed error, which linearly increases as the image distance increases. Since the synthetic data was proven to be accurate, this error must be a physical aspect to the camera that was not accounted for in the synthetically simulated plenoptic camera.

Chapter 4

Effect of a Flat Refractive Interface on Plenoptic Imaging and S_i Estimation

Throughout the previous phase of testing, the fact that the microlens array of the camera was fabricated out of a 10.4 mm thick pane of glass with an index of refraction of 1.517 was completely ignored. This preliminary data prompted a detailed look at how the imaging properties of the camera could be affected by a flat refractive interface along the line of sight for the plenoptic camera. One future application of the plenoptic camera is to image a porous flow in a refractive-index-matched facility, as detailed in Appendix A. A complication with imaging any fluid that is more dense than air, such as water, is the varying indices of refraction from the desired volume to the image sensor of the camera. This refraction causes a difference in magnification between an object and the image, as well as affects the depth estimation of particles. While the documented method of a mobile calibration grid would account for this distortion [2], the effects of the interface could potentially be addressed by a depth correction algorithm for the plenoptic camera. In addition to this, once the light passes through the camera, the refractive plate from which the microlens array is fabricated causes the light to once again change paths before passing through the microlenses. This refraction inside of the camera can potentially affect the magnitude of the magnification and lead to a misrepresentation of the depth of a particle in an illuminated field, just like an external refraction. Therefore, the effects of refraction must be studied both outside and inside the camera.

As discussed in the previous section, it is necessary to map a position on the image sensor x to its equivalent position on the aperture plane u. This relationship is given by

$$u = \frac{(x - x_c)S_i}{f_l} \tag{4.1}$$

where x is the distance of a pixel from the optical axis and u the distance of a point on the aperture from the optical axis. The pixel x_c is the location of the focal point of the microlens, determined through the calibration process described in Section 3.1.1. Since this relationship is based on geometry, Eq. (4.1) holds only as long as the light follows a constant path. This section discusses how the presence of a flat refractive interface impacts the relationship between the image space and object space, as well as the relationship between the pixels and the aperture of the camera.

4.1 Geometry of Tomographic Reconstruction

The location of the origin for a tomographically reconstructed volume is defined as the distance between the main lens of the camera and the nominal focal plane of the lens S_o, as seen in Figure 4.1. A particle in front of this focal plane has depth of $-\Delta z$, and a particle in behind this plane has a depth of Δz. The location of this origin is altered by a flat refractive surface located between the object volume and the camera, such as between a water tunnel and the surrounding air, and as such alters the positioning of the whole coordinate system. In addition to this, a refractive surface influences the mapping between each voxel and pixel, and can lead to improperly positioned particles relative to the origin. While this issue has been addressed with multiple-camera tomographic PIV, no analysis has been done for plenoptic PIV to correct these errors.

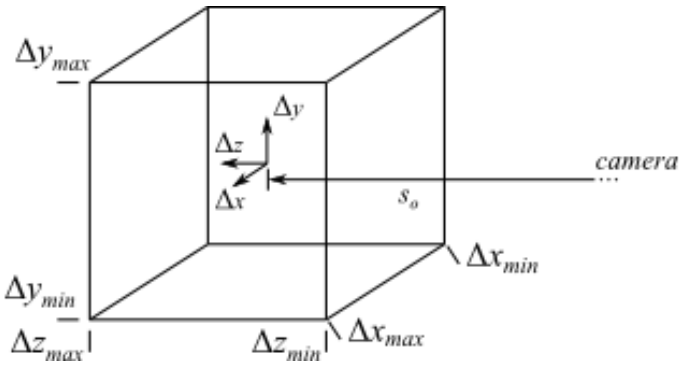

Figure 4.1: Coordinate system of a reconstructed volume.

Table 4.1: Effect of refraction on imaging equations

Refraction	Schematic	Imaging Equations
No Refraction	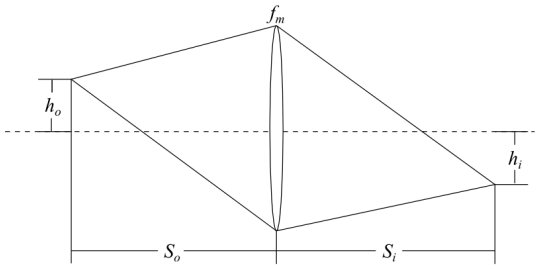	$\frac{1}{S_o}+\frac{1}{S_i}=\frac{1}{f_m}$ $M=-\frac{h_i}{h_o}=-\frac{S_i}{S_o}$
External Refraction	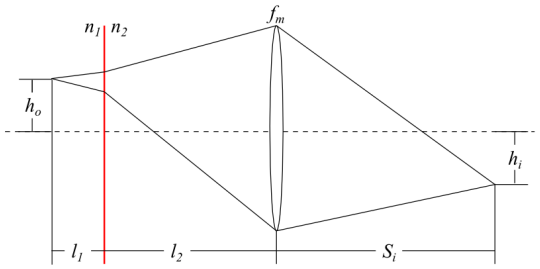	$\frac{1}{\frac{n_2}{n_1}l_1+l_2}+\frac{1}{S_i}=\frac{1}{f_m}$ $M=-\frac{h_i}{h_o}=-\frac{S_i}{\frac{n_2}{n_1}l_1+l_2}$
Internal Refraction	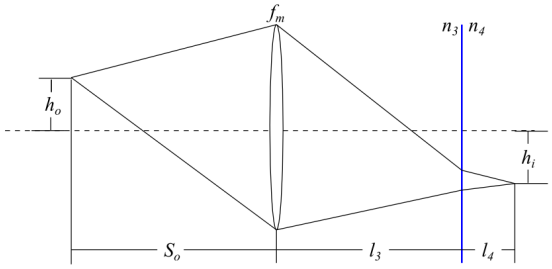	$\frac{1}{S_o}+\frac{1}{l_3+\frac{n_4}{n_3}l_4}=\frac{1}{f_m}$ $M=-\frac{h_i}{h_o}=-\frac{l_3+\frac{n_4}{n_3}l_4}{S_o}$
Combined Refraction	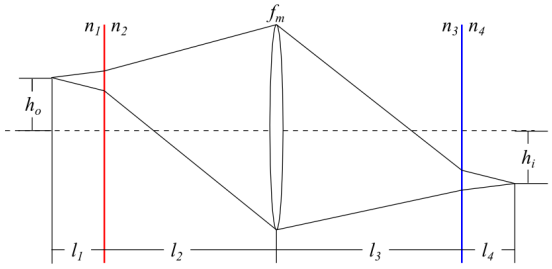	$\frac{1}{\frac{n_2}{n_1}l_1+l_2}+\frac{1}{l_3+\frac{n_4}{n_3}l_4}=\frac{1}{f_m}$ $M=-\frac{h_i}{h_o}=-\frac{l_3+\frac{n_4}{n_3}l_4}{\frac{n_2}{n_1}l_1+l_2}$

4.2 Analytical Estimation of the Effect of a Flat Refractive Interface

The presence of a flat interface within the optical path from a point in object space to a point in image space was modeled using ray transfer matrices, also commonly known as ABCD matrix analysis [29]. Ray transfer matrices provide a convenient method to study

the combined effects of multiple elements in the optical path of the system on the position x and direction of propagation θ of a light ray. Since a flat refractive interface only alters the direction of propagation of a ray, the interface can be simply modeled by the ray transfer matrix

$$\begin{bmatrix} x_{out} \\ \theta_{out} \end{bmatrix} = \begin{bmatrix} 1 & 0 \\ 0 & n_2/n_1 \end{bmatrix} \begin{bmatrix} x_{in} \\ \theta_{in} \end{bmatrix} \tag{4.2}$$

From the ray transfer matrices, the unique imaging relationship for a given optical system can be determined. Four possible configurations were analyzed and are shown in Table 4.1: a) a simple thin lens relationship; b) a refractive interface contained in the object space; c) a refractive interface contained in the image space; and d) a refractive interface contained in both the object space and the image space. Table 4.1 also includes a schematic of each relationship, showing the location of the refractive interface and the distances between each element. With the presence of the refractive interface, the distance between the main lens and the focal point was subdivided into l_n before the interface and l_{n+1} after the interface. Next to each schematic is the corresponding imaging equations that relate a point in the object space to a point in the image space. The equations were rearranged as the sum of the inverse distances to the main lens in order to illustrate the analogous behavior to the thin lens equation and the distances associated with a flat refractive interface. As such, the effective object and image distances can be defined as follows:

$$S_{o,\text{eff}} = (n_2/n_1)l_1 + l_2 \tag{4.3}$$

$$S_{i,\text{eff}} = l_3 + (n_4/n_3)l_4 \tag{4.4}$$

The magnification of an optical system is still determined by measuring the ratio of the height of ruler on an image sensor to the actual height of the ruler in the object space.

Rather than being directly equated to the physical distance of the focal plane from the main lens, the magnification can also be shown to be equivalent to the effective values of S_i and S_o, as shown in Table 4.1. This demonstrates that the relationship between the image sensor and the main lens of the plenoptic camera can be expressed as

$$u = \frac{(x - x_c)S_{i,\text{eff}}}{f_l} \tag{4.5}$$

This mapping provides a convenient representation to build the light field directly from previously established methods. This shows that the construction of the light field implicitly assumes an image space void of a refractive interface.

In plenoptic PIV, a grid is constructed in object space upon which the volume reconstruction is formulated. As the light-field is captured and parameterized in image space, the desired grid in object space must be mapped to its corresponding grid in image space. The thin lens equation has been proven to provide a convenient means of performing this mapping, but the refractive interface complicates this relationship, as shown in Table 4.1. Therefore, a coordinate transformation must be implemented between the physical coordinates of the volume and the effective coordinate system as given by the reconstruction process. For reconstruction, the depth of a particle Δz is defined by the distance from the nominal focal plane $S_{o,\text{eff}}$. While the location of the nominal focal plane accounts for the refraction, the relative depth for out-of-plane particles does not account for any refractive effects. Using the nominal focal plane of the main lens as a reference, a grid can be constructed by mapping points that are shifted relative to this plane in the depth direction as follows:

$$S_{o,\text{eff}} + \Delta S_{\text{eff}} = (n_2/n_1)(l_1 + \Delta z) + l_2 \tag{4.6}$$

This can then be simplified to

$$\Delta S_{\text{eff}} = (n_2/n_1)\Delta z \tag{4.7}$$

In these equations, Δz represents the physical distance in object space and ΔS_{eff} is the change in effective object distance. This can be understood by considering the imaging of an object in a water tunnel, where the presence of the interface results in a magnification that is proportional to the index of refraction of water. In a similar manner, a flat refractive interface within the camera can also lead to a misrepresentation of the proper depth of a particle. Unlike the external refractive interface, the effect of the internal interface on the depth of a particle cannot be easily correlated through the imaging equations. Moreover, particles may be focused both in front of and behind the refractive interface. Particles that impact the refractive interface after passing through the lens focal point will have a different magnitude of distortion than particles that pass through the interface and then are focused to a point. Thus, a noticeable discrepancy between the depth estimation of particles across these two regimes is expected.

In summary, the raw data recorded by the plenoptic camera is rendered into a light field measurement by determining, for each pixel on the image sensor, the corresponding point of intersection on the microlens plane and the aperture plane. This rendering process relies on a measurement of the imaging system's nominal magnification and a simple calibration to determine the center of the aperture microlens images. The rendering process, however, implicitly models the image space of the camera as being free from refractive interfaces such that the distance S_i is an effective distance, not a physical distance actually contained within the camera. This distance, in turn, is mapped to the outside world by the thin lens equation. In the case where a refractive interface is also present in the outside world, the mapping generates an effective object distance which can be related to the real object distances by Eq. (4.6).

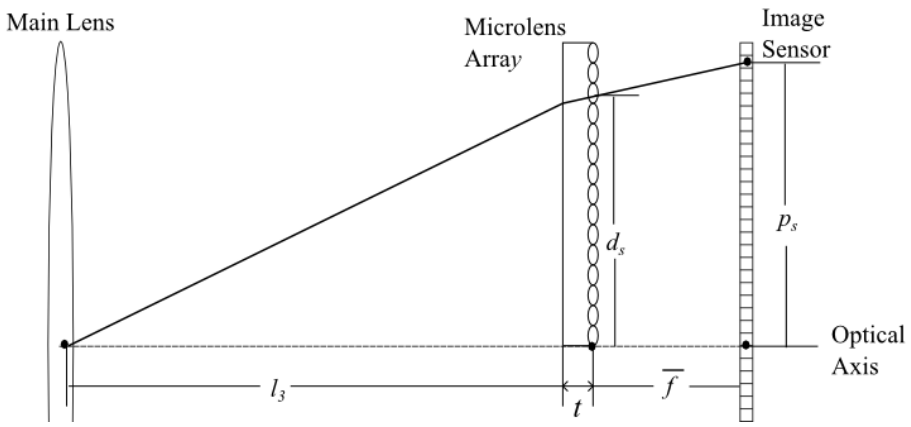

Figure 4.2: Path of a light ray through a plenoptic camera with a flat refractive interface.

4.3 Adjustment to Focal Point Algorithm

With the addition of a flat refractive interface, Eq. (3.11) no longer equates the position of a microlens to the position of the corresponding focal point. The new geometry for the light entering through the center of the aperture is shown in Figure 4.2. Similar to the geometry shown in Section 4.2, the interior of the camera is divided into two main sections: from the main lens to the refractive interface, and then from the refractive interface to the focal point of the lens. For the plenoptic camera, this main lens focal point is at the microlens plane, which is located at a distance t behind the refractive plane. The light entering the camera propagates in a straight line from the center of the camera to a point on the refractive plane. There, the light is bent by a factor of the refractive index, and then propagated to the microlens array. Since the optics of a microlens are fabricated such that light passing through the center of the lens will not bend, there is no need for a second interface to be modeled at the microlens array. Instead, the light continues at the same angle of incidence until the image sensor is impacted.

By using ray transfer matrices once again [29], the relationship between the microlens array and the image sensor may be determined geometrically to be

$$p_{s,\text{est}} = \left(1 + \frac{\overline{f}}{nl_3 + t}\right) d_s \tag{4.8}$$

A full derivation of this equation is shown in Appendix B. Rather than determining the image distance S_i from this equation, the physical distance l_3 is found instead. From here, Eq. (4.4) must be used to determine the effective value of this image distance. For the plenoptic camera, l_4 is equivalent to the thickness of the glass plate, such that

$$S_{i,\text{eff}} = l_3 + nt \tag{4.9}$$

To implement this new algorithm, only the relationship equation needs to be changed to Eq. (4.8). The value output by the code must then be corrected to reflect the effective image distance.

Chapter 5

Validation of Depth Correction and Image Distance Correction

With the realization of the existence of a flat refractive interface within the camera, adjustments had to be made to the estimation of both the image distance from the focal points and the depth of a reconstructed particle. The magnification method for determining the image distance was unaffected by this development. The alterations to the particle depth simulation were verified first to confirm the basic understanding of the impact of the flat refractive interface. Following this, the new image distance algorithm was tested for both accuracy and robustness.

5.1 Simulation Design for Depth Estimation

A refractive interface in the optical path is known to have an effect on the estimated depth of a particle in a volume, but the magnitude of these effects had yet to be classified. To verify the depth correction equation, presented in Eq. (4.7), a series of simulated plenoptic images were generated for a particle located at different depths along the optical axis, once again using the program ALFA. By placing the particle along this axis, variations in the horizontal and vertical components were made negligible. A 50 mm lens was modeled with a magnification of -1, such that $S_{o,\text{eff}} = S_{i,\text{eff}} = 100$ mm. The experimental design was divided into three separate optical arrangements: no refractive interfaces along the optical path, a refractive interface between the object and the volume, and a refractive interface in front of the microlens array. The first simulation in each set placed the particle at 10 mm in front of the focal plane, and the particle was shifted away from the camera in 1 mm increments until the particle was 10 mm behind the focal plane. This range was chosen due to the higher accuracy of the tomographic reconstruction process within the region. The first set of

simulations, generated without any refractive interfaces, was completed to provide a baseline for improvement and to demonstrate the accuracy of the reconstruction algorithm. Images were then simulated with a refractive interface of magnitude $n = 1.33$, positioned 40 mm in front of the effective focal plane, such that $l_1 = 40.00$ mm and $l_2 = 69.92$ mm as determined by Eq. (4.3). The resulting reconstructed particles were expected to be compressed toward the focal plane when compared with the actual simulated position. By applying Eq. (4.7) to the simulated positions, the new locations were expected to align with the actual position of the particle. Finally, a glass plate was simulated in front of the microlens array with an index of refraction of $n = 1.46$ with a thickness of $t = 6.3$ mm, such that $l_3 = 95.68$ mm and $l_4 = 6.30$ mm based on Eq. (4.4). The effect of the refractive plate was expected to be accounted for by the magnification method for determining the image distance.

5.2 Corrections for Depth Estimation

In order to reduce the computation time, the simulated volume was reconstructed as a 50 x 50 x 120 voxel grid, such that each square voxel was roughly 0.125 mm in length. For the horizontal and vertical directions, the reconstruction volume spanned from -3 mm to 3 mm in both directions. All reconstructed particles were within 0.2 mm of the optical axis. For the depth, the volume of interest spanned 15 mm, where the range was adjusted such that the particle should not be reconstructed within 5 mm of the edge of the volume to verify accuracy.

As discussed in previous studies on plenoptic PIV [27, 16] and in Section 2.4, reconstructed particles are elongated in the depth direction due to the limited parallax of the plenoptic camera. A centroid method was used to determine a precise particle location for each reconstruction. Preliminary results showed that the inclusion of a refractive interface between a particle and the camera visibly altered the estimated depth of a particle. Figure 5.1 exhibits two reconstructed particles that were simulated at the same depth 10 mm behind the focal plane, one without an interface and one with the refractive surface. The

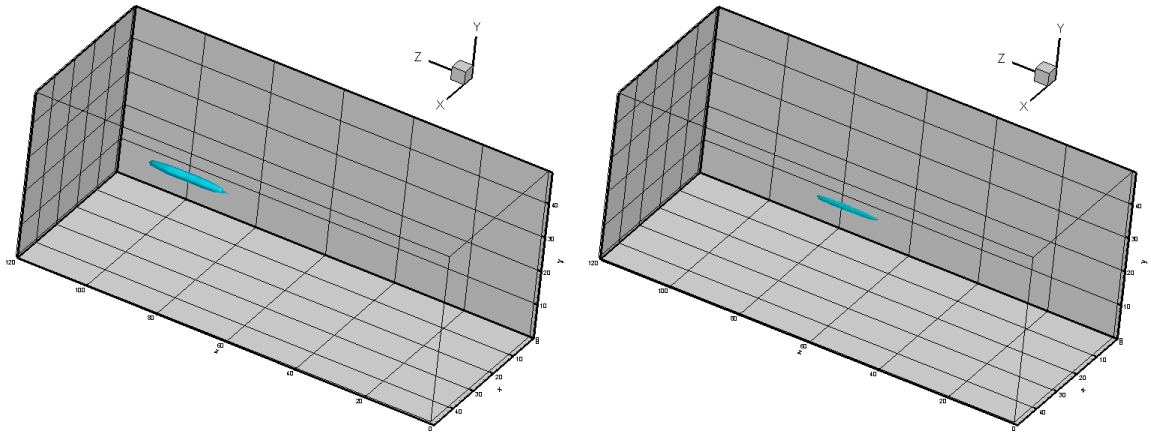

(a) No refractive interface (b) External refractive interface

Figure 5.1: Reconstructed position of a particle simulated at the same depth.

camera was positioned to the right of each of the volumes, and the reconstructed depths represent the range from 0 mm to 15 mm. It can be clearly seen that the particle simulated with a refractive interface is significantly closer to the nominal focal plane, at a visual disparity of around 20 voxels with the non-refractive reconstruction.

In order to validate Eq. (4.7) for reconstructions involving a refractive interface between the volume and the camera, each simulated image was reconstructed based on the known magnification and assuming no refractive interfaces. The reconstructed position of each particle was plotted against the actual simulated position, where the nominal focal plane is the origin. These results are compared with the a theoretical perfect reconstruction in Figure 5.2, represented by the black line. The blue line plots the reconstruction of the images generated without any refractive interfaces to demonstrate the accuracy of the reconstruction algorithm. In Figure 5.2(a), as expected, the red line shows that the reconstruction of particles behind a refractive interface causes each particle to be compressed toward the focal plane. The error in location increases with distance from the focal plane. In Figure 5.2(b), where the position of the particles is corrected in accordance with Equation 4.7, the depths of the particles behind an interface align nearly perfectly with the particles without any interfaces. A linear fit was applied to each optical arrangement, with the properties shown in Table 5.1. This simulated experiment demonstrated two key confirmations for the analytical

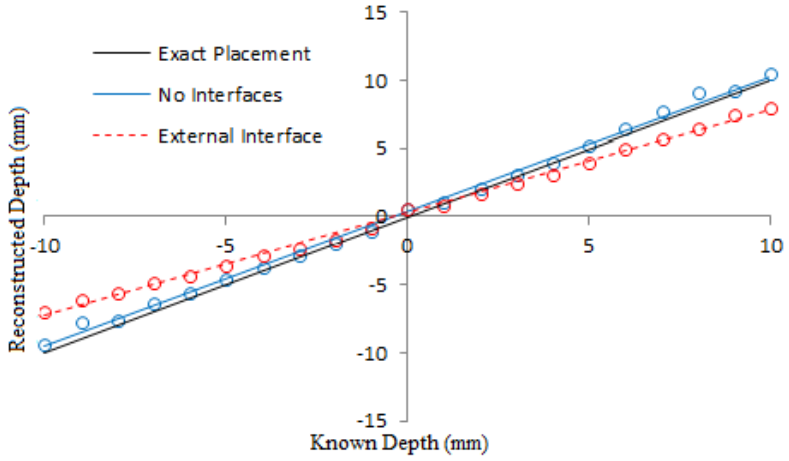

(a) Raw reconstructed position

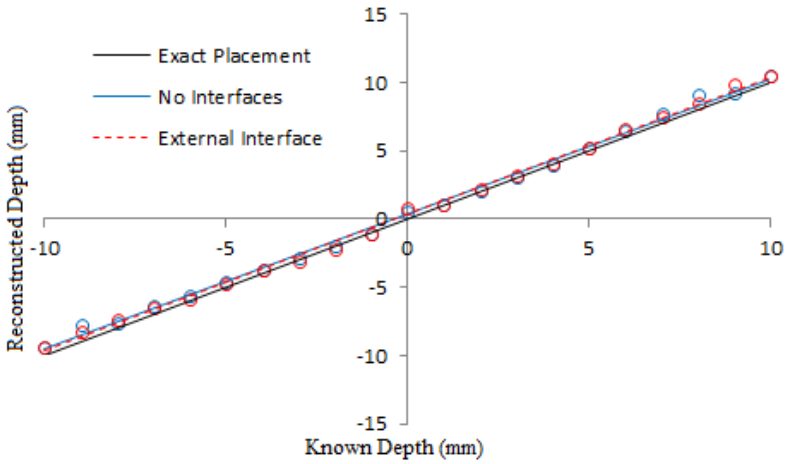

(b) Correction for refraction

Figure 5.2: Reconstructed position versus known position from $-10\text{mm} \leq \Delta z \leq 10$ mm

Table 5.1: Effect of refraction corrections

	Without Refraction	Exterior Interface Uncorrected	Exterior Interface Corrected	Internal Interface Uncorrected	Internal Interface Corrected
Slope	0.9925	0.7563	1.0059	1.4265	0.9770
Intercept	0.3675	0.2694	0.3583	-0.3176	-0.2175
R^2 value	0.9971	0.9975	0.9975	0.9939	0.9939

solution. First, the error in depth caused by the refractive interface does not have to be adapted into the tomographic reconstruction process, but can simply be applied to a volume during post-processing. Second, the intercept for even the uncorrected refraction was shown to be near zero. This shows that using an effective S_o to define the volumetric coordinate system with an interface will yield a similar reconstruction to the same volume without an interface.

The final series of simulations involved an internal refractive plate with an index of refraction of $n = 1.46$. Figure 5.3 compares the results of the reconstruction without any interfaces to the position of the particle reconstructed with an internal interface, shown in green. Only the range between $-5 \leq \Delta z \leq 5$ mm is shown for this case, since the discontinuties begin to occur outside of this range. Like the external interface, a linear fit may be applied to the particles reconstructed with an internal interface. These properties are also shown in Table 5.1. Once again, the slope of the reconstructed particles is directly proportional to the index of refraction of the plate. From the resulting data, the depth of a particle may be corrected by dividing by the index of refraction of the internal interface, such that

$$\Delta S_o = (n_3/n_4)\Delta z \tag{5.1}$$

Figure 5.3(b) shows the reconstructed position with the correction applied. Once again, the corrected position closely matches the accuracy of the reconstruction without any refractive interfaces. In addition to this, the range of reconstructed particles from $0 \leq \Delta z \leq 10$ mm

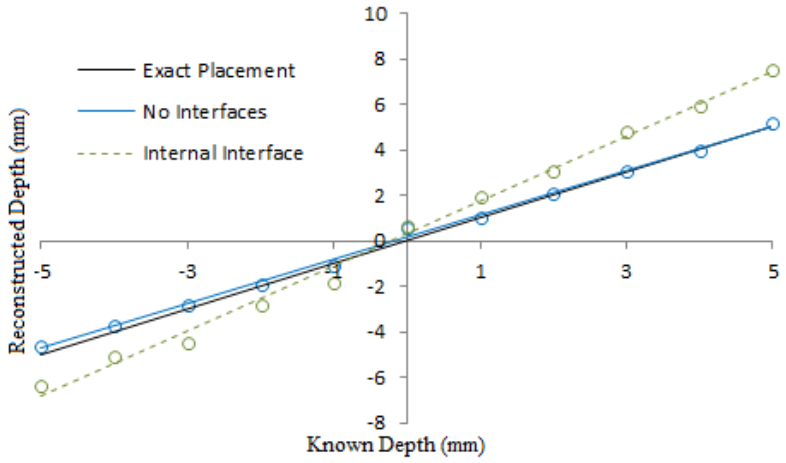

(a) Raw reconstructed position

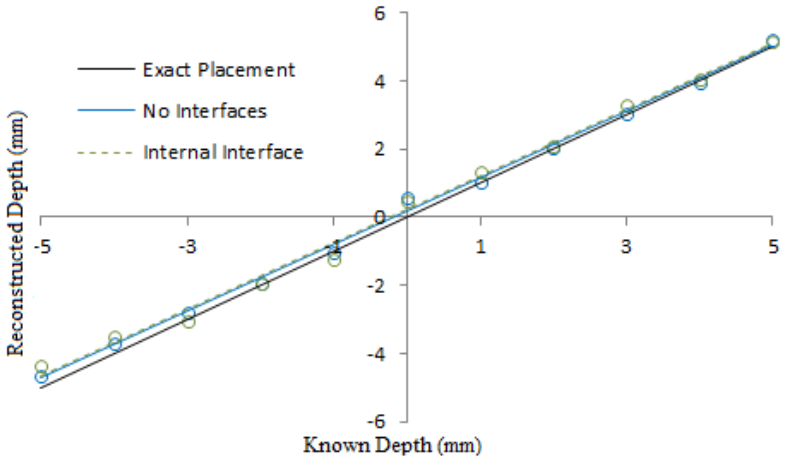

(b) Correction for refraction

Figure 5.3: Reconstructed position versus known position from $-5\text{mm} \leq \Delta z \leq 5$ mm.

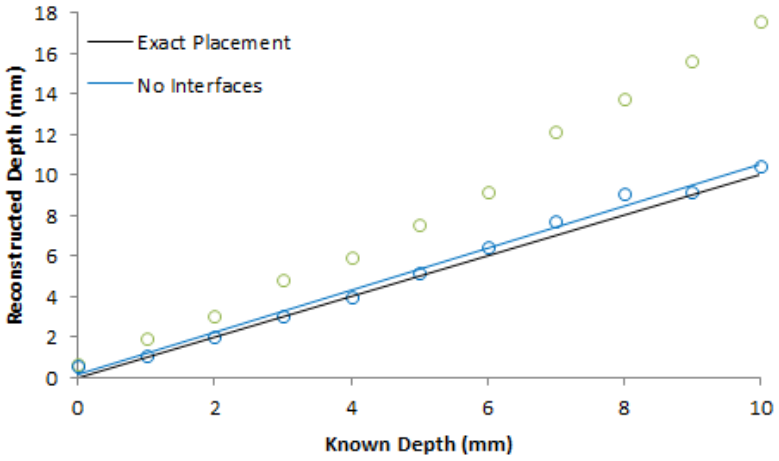

Figure 5.4: Reconstructed particle position from $0 \leq \Delta z \leq 10$ mm with an internal interface.

is shown in Figure 5.4. There is a significant deviation in the depth reconstruction around 7 mm, with the properties shown in Table 5.2. The error in the position of the particles at a depth greater than the 7 mm discontinuity do not show any error trend that may be correlated to the index of refraction, and thus a correction equation for these particles cannot be generated from known quantities as was done for in Eqs. (4.7) and (5.1). Further study will be needed to properly correlate these particles to the proper position, but the cause is possibly associated with the particles being focused in front of the refractive plate, rather than to a point within or behind the glass.

5.3 Synthetic Test for New Focal Point Model

Similar to the original synthetic testing, a series of focal point calibration images were generated through a modified version of the Auburn Light Field Analyzer, which will now model a camera with a glass plate in front of the microlens array. For this secondary testing,

Table 5.2: Discontinuity with particle in front of internal interface

	Without Refraction	Particles Focused Behind Interface	Particles Focused In Front of Interface
Slope	0.9925	1.4162	1.8026
Intercept	0.3675	-0.4911	0.5211
R^2 value	0.9971	0.9964	0.9984

the magnification was once again varied from a value near 0 to 2. All properties of the camera remained the same, except for the inclusion of a glass plate with a thickness of 6.3 mm and an index of refraction of 1.46. These values were originally thought to be the dimensions of the plate within the camera, until further discovery showed that the actual depth was 10.4 mm with an index of refraction of 1.517. Although different magnitudes from what is expected in the experiment, this synthetic test was still able to prove the concept of refraction correction.

The calibration images generated by ALFA were also analyzed using the original model equation in order to compare the accuracy of the improved focal point calibration algorithm to the original implementation. The blue data points in Figure 5.5 show the error generated by the previous method when an interface is present. The previous model grossly overestimates the length of the image distance, just as the experimental results in Section 3.2.5 showed. When the proper relationship equation is implemented, however, the resulting values align precisely with the known values for the image distance, with an accuracy akin to the previous synthetic results. This demonstrated that the new relationship equation correctly accounted for the refraction caused by a glass pane and also showed that the refractive interface was a probable cause for the large error seen in the original experiments.

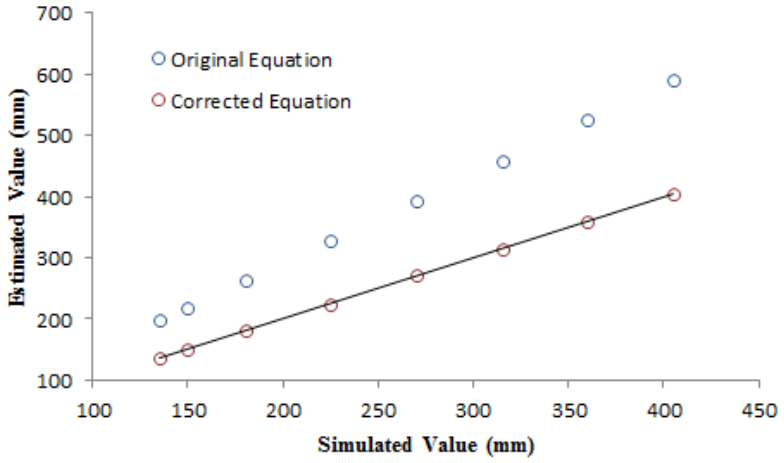

Figure 5.5: Synthetic results for a 135 mm lens with refractive plate.

Table 5.3: Synthetic noise error for different image distances with a 135 mm lens

Noise (% of pixel)	135 mm	270 mm	405 mm
0	0.02	0.03	0.01
33	0.04	0.11	0.25
67	0.00	0.77	0.80
100	0.11	0.27	0.68

While a synthetically generated microlens array has perfect pitch, the known error in positioning for the microlenses in the physical array is a non-cumulative ± 3 μm. To test the robustness of the algorithm for the slight variance in microlens center locations, random noise was added to the location of each focal point. The largest magnitude of variance that was tested was varied over the range of $[-7.4\ 7.4]$ μm, which corresponds to plus or minus one pixel width. The results for three of the simulated calibration images are shown in Table 5.3. The general trend shows that optics with a large image distance are more sensitive to the random fluctuations in pitch, but overall the algorithm provided accurate results in all cases, with the error being within a millimeter.

5.4 Experimental Arrangement

The basic premise behind the focal point method for calibration is the relationship between the location of a point on the microlens array to the focal point of that microlens. While a synthetic array has perfect pitch between each of the microlenses, the manufactured array is reported to have a pitch variance of $\pm 3\%$. While the noise error tests demonstrate that the algorithm is capable of compensating for this variance with only a small error, the accuracy could be further improved by determining the precise location of the centers of the microlenses within the array. This may be done during the alignment process for the microlens array that is detailed in Section 2.5, when all lenses are removed and collimated light is shined directly onto the array. The light impacting the array should be perpendicular to all points along the array, causing all microlens focal points to lie directly beneath the

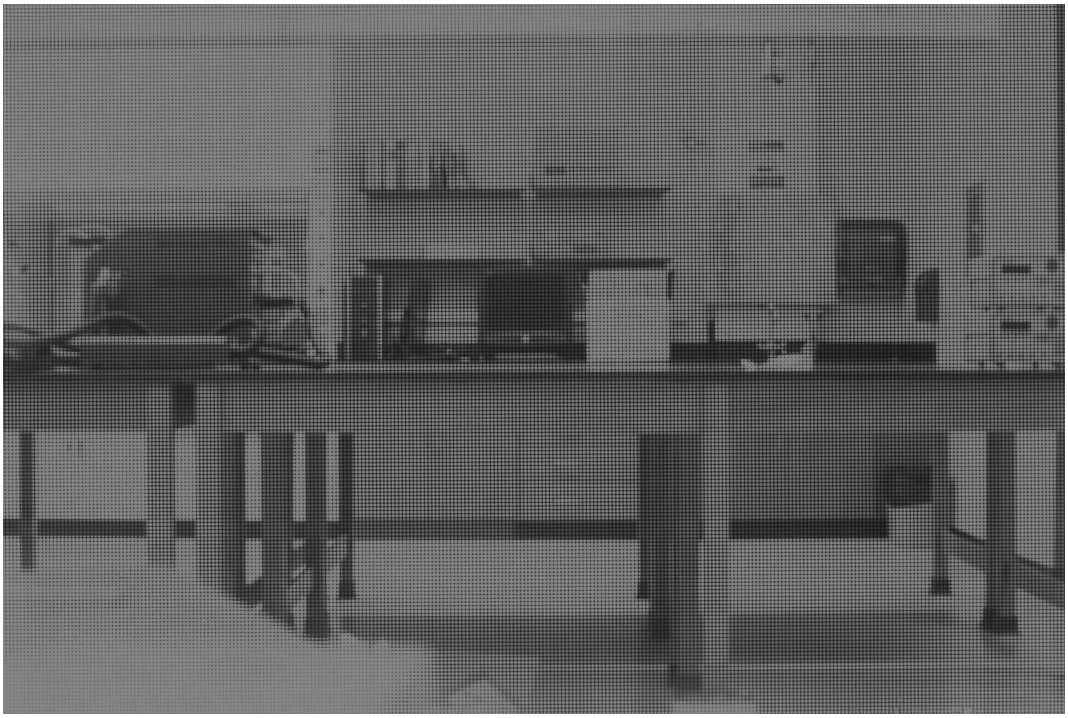

Figure 5.6: Magnification image near optical infinity for a 50 mm lens.

center of the microlenses. The location of the centroid of each focal point on the image sensor (s, t) can then be directly used as the location of the microlens centers $(s, t, \overline{f})$.

Both a Nikkor 50 mm and a Nikkor 135 mm manual focus lens were used in order to experimentally examine a wide range of image distances. A series of extension tubes were implemented to incrementally increase the image distance of the plenoptic camera. For each lens, a large box with clearly defined edges and known width was placed as far away from the camera as possible so that the magnification of the camera could be determined near optical infinity, as shown in Figure 5.6. The focus setting of the lens was then changed until the white box appeared in focus, and the magnification method was used to estimate the the image distance. The image distance measured was expected to be close to the focal length of the lens for this case, although slightly increased due to the change in focus. This S_i was used to provide a baseline estimate for the change in image distance as extension tubes were added to the camera. The length of an extension tube directly correlates to the change in image distance, such that a 12 mm extension tube should cause a 12 mm change

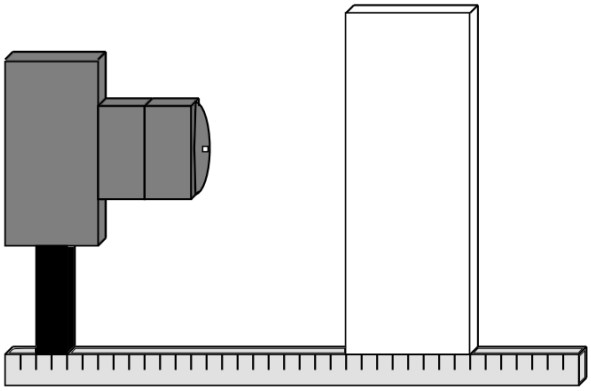

Figure 5.7: Simple experimental set-up.

in S_i. By performing the experiment in this manner, the image distance provided by both the magnification method and the focal point method could be compared to the known value determined from the baseline S_i plus the total length of extension tubes. After the baseline images were taken, with both a magnification image and a microlens focal point image, this process was repeated for combined extension tube lengths of 12 mm, 24 mm, 36 mm, 48 mm, 60 mm, 76 mm, 88 mm, and 100 mm, with the focal point calibration image arrangement shown in Figure 5.7. When each extension tube was added, special care was taken to ensure that the focus of the lens was not altered. Therefore, for the magnification method, objects were moved until the focal plane was found, rather than adjusting the focus setting of the lens.

5.5 Experimental Testing of Both Methods

First, the accuracy of the magnification method for determining the image distance was examined. The value of the image distance provided by the magnification method is compared with the image distance based on the length of the extension tubes in Figures 5.8 and 5.9. The magnification method is shown to provide an excellent estimate for the image distance for all range of values, although some small error may be seen in some cases. Additionally, the standard deviation in the error appeared to remain constant at all image

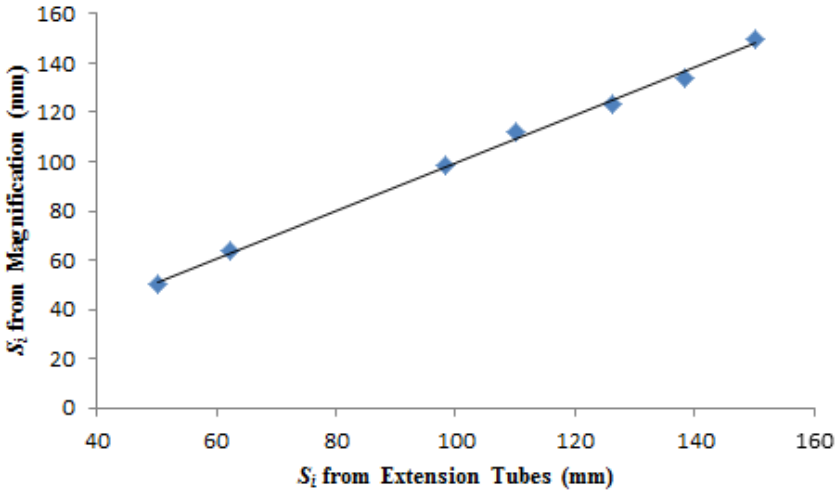

Figure 5.8: Magnification method accuracy for a 50 mm lens.

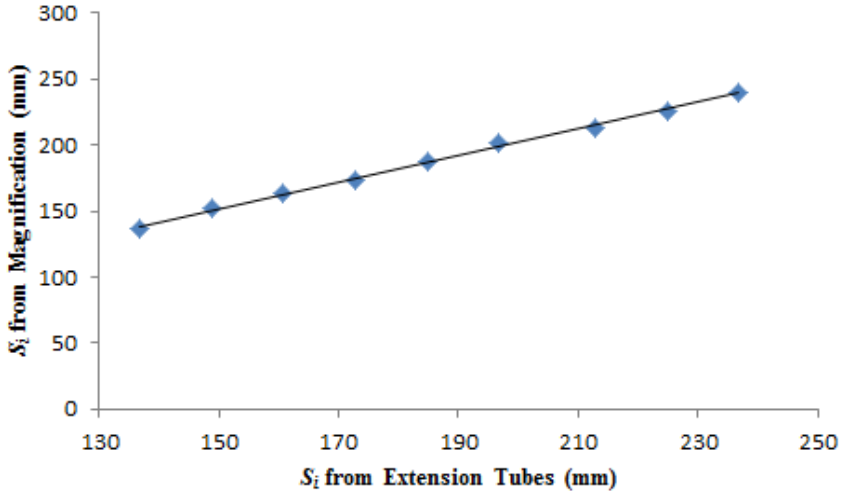

Figure 5.9: Magnification method accuracy for a 135 mm lens.

distances rather than showing any increasing or decreasing trends. For the 50 mm case, the focal point calibration images were corrupted for the extension tubes lengths of 24 mm and 36 mm, or where the image distance equaled 74.26 mm and 86.26 mm respectively. For both the magnification and the focal point methods, these two data point are not included. All values of the magnification method were within 5 mm of the expected result for both the 50 mm and the 135 mm lenses. A full study on the trends of this error will be presented in Section 5.7.

For the focal point method of calculating the image distance, the distance between the microlens array and the image sensor was assumed to be a nominal $\overline{f} = 500$ μm. The tilt of the array estimated by the alignment image was shown to be accurate to within 10^{-4} for all cases. The positioning offset in the vertical direction was within 3% of the microlens width; however, in the horizontal direction this offset was closer to 10% of the microlens width. This may have been caused by the light passing through the array at a small angle, since Schlieren mirrors were used to redirect the light. This error is still small and should not have a significant impact on the validity of the results, but care should be taken in the future to better orchestrate proper alignment. The computed image distance for the experimental cases is compared with the known value for the 50 mm and 135 mm lens cases in Figures 5.10 and 5.11 respectively. While the original experiment shows that the calculated image distance was greater than the known value, the corrected equations now underestimate this distance by a similar margin. This error was initially attributed to a small variation in the distance $\overline{f}$, but further analysis showed that the calculated values of the image distance would only converge to the known solution when $\overline{f} = 900$ μm, well beyond the possible range of error in microlens array placement.

Table 5.4: Linear trends for the error in image distance

	50 mm lens	135 mm lens
Slope	0.5149	0.5309
Intercept	-39.734	-22.236
R^2 Value	0.9994	0.9992

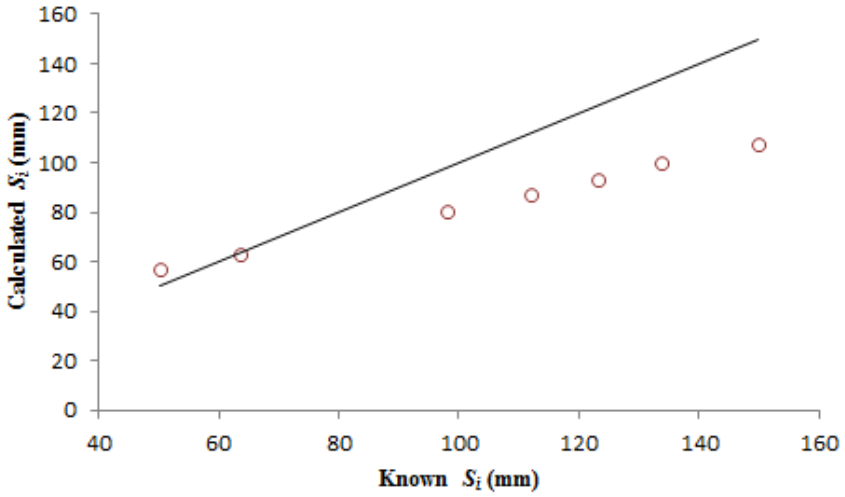

Figure 5.10: Experimental results for image distance prediction for a 50 mm lens.

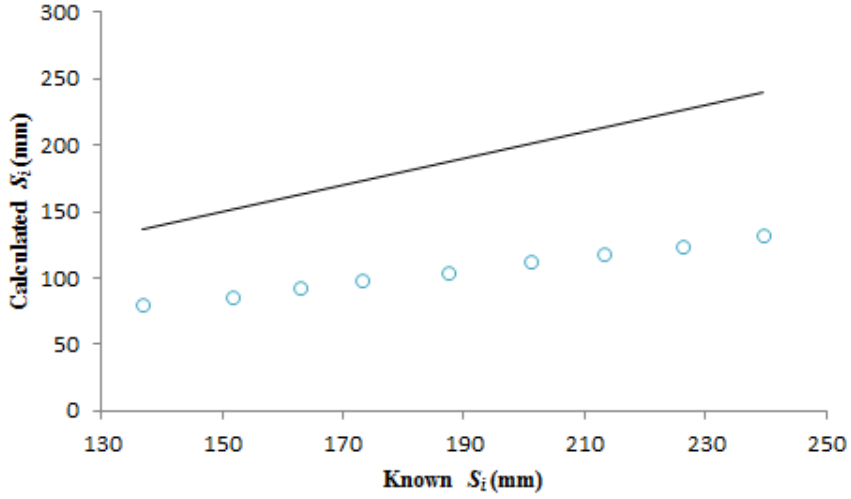

Figure 5.11: Experimental results for image distance prediction for a 135 mm lens.

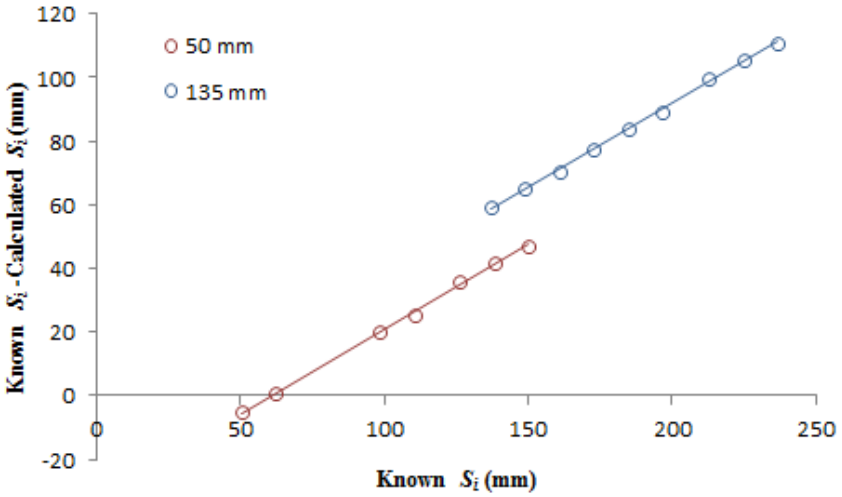

Figure 5.12: Differences between the known and computed values for the image distance.

The difference between the known value for the image distance and the calculated value was plotted in order to ascertain if there was any noticeable trend to the error. This plot is shown in Figure 5.12. For both the 50 mm and 135 mm lens cases, the magnitude of this distance linearly increases as the image distance increases; however, the 135 mm lens data points are not a continuation of the 50 mm lens data points. The values associated with each trend line are shown in Table 5.4. While the slopes for the differences in each lens are similar, the intercept value is highly varied. Furthermore, the ratio between the differing intercepts is not equivalent to the ratio between the focal lengths of the corresponding lenses. Since the error is different for each lens, the cause of the offset is likely due to a specific property of each lens, rather than a problem with the model itself.

For both the 50 mm and 135 mm lens cases, this linear trend may be represented by the equation

$$S_{i,\text{corr}} - S_{i,o} = a * S_{i,\text{corr}} + b \tag{5.2}$$

where $S_{i,\text{corr}}$ is the correct value of the image distance, $S_{i,o}$ is the computed value, and a and b are the linear fit constants. From Eq. (5.2), a correction may derived for each lens that

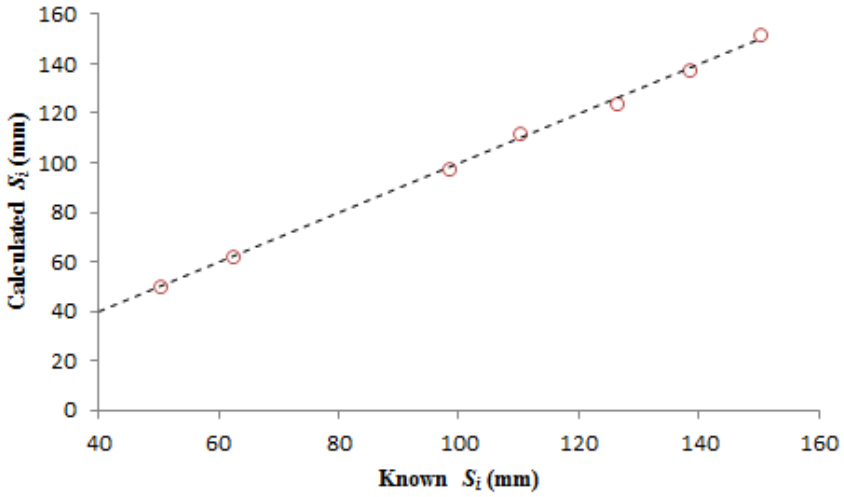

Figure 5.13: Experimental results corrected for error for a 50 mm lens.

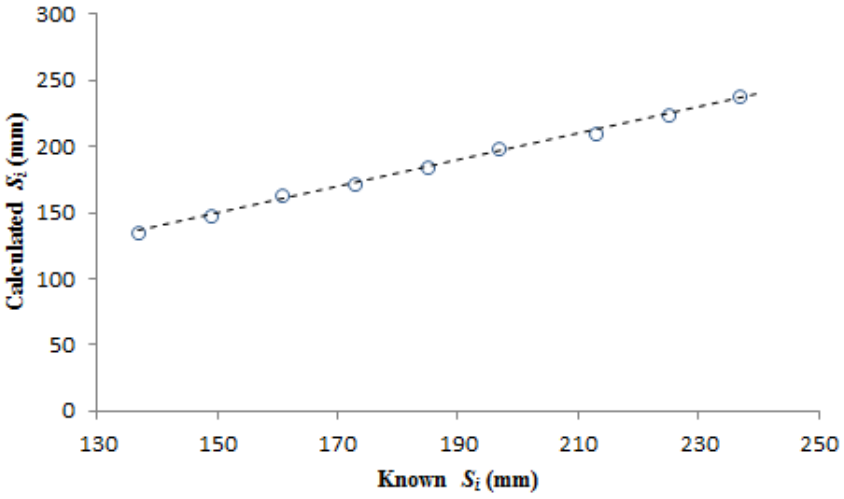

Figure 5.14: Experimental results corrected for error for a 135 mm lens.

would properly estimate the image distance based on the computed result. These corrective equations were found to be

$$S_{i,\text{corr}} = 2.0614 S_{i,o} - 81.9089 \tag{5.3}$$

for the 50 mm lens, and

$$S_{i,\text{corr}} = 2.1317 S_{i,o} - 47.4014 \tag{5.4}$$

for the 135 mm lens. Figures 5.13 and 5.14 show the estimations for the image distance compared with the known distance, this time with the correction applied to the computed result. For both lenses, the corrected computed values provide an excellent representation of the image distance.

5.6 Effect of Uncertainty in Microlens Array Positioning

One possible cause for the increasing error in the image distance estimation as the image distance increased is the uncertainty in the microlens array placement. As stated in Section 2.5, the placement of the microlens array in the plenoptic camera has an uncertainty in location between ± 25 μm, which corresponds to $475 \leq \overline{f} \leq 525$ μm. Naturally, this has the potential to cause noticeable differences in the measured magnitude of the image distance. The uncertainty was found by geometrically calculating the average spacing between the focal points for a given value of the image distance, first with $\overline{f} = 525$ μm and then $\overline{f} = 475$ μm. For both pairs of the average spacing, the magnitude of the image distance was deducted as though the value of the array alignment matched the expected value of $\overline{f} = 500$ μm. The resulting uncertainty is shown in Figure 5.15. This uncertainty is far from insignificant, but is notably a linear function with regard to the image distance. As such, this positioning uncertainty is at least a portion of the overall error that is compensated for in the correction equations required by the lens geometry.

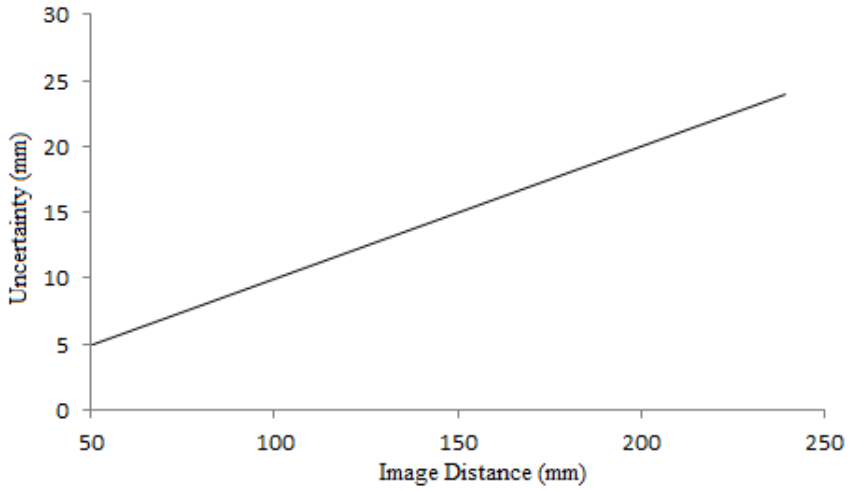

Figure 5.15: Uncertainty caused by imprecise microlens array placement.

5.7 Error Analysis

Figure 5.16 shows the lens design for one of the Nikkor lenses that were used in this experiment. For analytical purposes, the lens modeled in this method was assumed to be a thin lens. For the geometric properties such as focal length and magnification, this is a valid assumption that is built into the complex lens design. For precise measurement of distances, however, the full optics of the lens must be considered. For a complex lens, the aperture stop of the lens is placed at the geometric center of the lens, from where the focal length of the lens is also determined [31]. For the algorithm described above, the light is assumed to propagate from this location in a straight line until the microlens array is impacted. As seen in Figure 5.16, the light is instead passed through further optics before being propagated through free space. This is a highly plausible cause for the error seen in the experimental results.

This optically-induced error can be explained by examining a standard six optical element lens, whose properties were detailed by Smith[32]. This lens has three elements in front of the aperture plane and three elements behind the aperture plane. The focal length of this lens is 100.7 mm, and the design of the lens was provided with enough detail to perform a ray transfer analysis for light passing through the lens with a stopped down aperture.

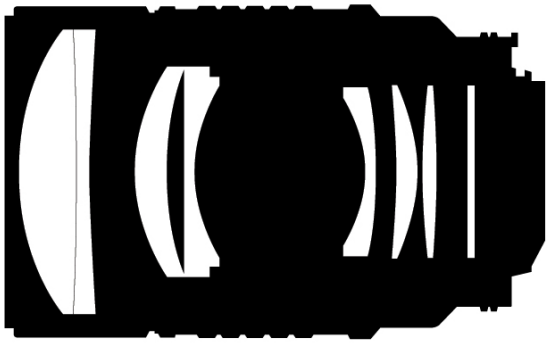

Figure 5.16: Lens design for a Nikkor 135 mm f/2D lens [30].

Figure 5.17 shows light passing through this lens with an f-number of $f/16$, the same as was used in the experimental testing. After the light passes through the stopped down aperture at the optical axis, the light continues to narrow until it is brought to a focus right behind the rear element of the lens. For the focal point method of calibration, however, the light was assumed to propagate in a straight line from the aperture to the image sensor. The red dotted line shows the error in approximation caused by this fallacy, which for the case shown, lies short of the aperture plane.

When an extension tube is added onto a lens mount, the distance between the end of the lens and the image sensor is effectively increased. The new image distance is still measured by adding the length of the extension to the previous value of the image distance. Since the image sensor is further away from the camera but the image sensor maintains the same dimensions, the angle of incidence of the light on the image sensor is at a different angle than before. In order for the focal point method to have a constant error as the image distance is increased, the estimated value of the image distance should remain at the same point relative to the lens. As seen in Figure 5.18, however, a gap appears between the rear element of the lens and the predicted value of the image distance. This shows to be a probable reason for

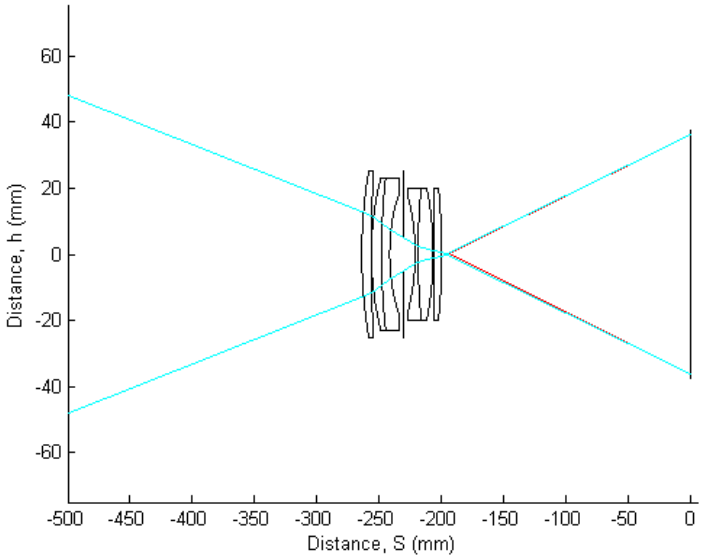

Figure 5.17: Design of a complex lens.

the error in the image distance estimation to be increasing as the actual value of the image distance increases.

Furthermore, the linearity of the error when the full lens is moved can be explained by looking at the space between the rear element and the image sensor, as seen in Figure 5.19. This image sensor plane for a conventional camera is equivalent to the microlens array of a plenoptic camera, as both determine the spatial resolution of the image. Figure 5.19 shows a microlens located at point s, which is a horizontal distance w from the edge of the rear lens element. When an extension tube is added, the back focal length bfl of the camera is increased by the length of the extension tube x. This increase changes the angle of incidence of the light on that microlens, but the positioning of the microlens remains unchanged. Because of this, the magnitude of the calculated image distance is also increased, but by a different scale factor labeled y in Figure 5.19. The relationship between a change in the back focal length of the camera to the change in the calculated image distance is given through similar triangles as

$$y = \frac{S_{i,\text{calc}} x}{\text{bfl}} \tag{5.5}$$

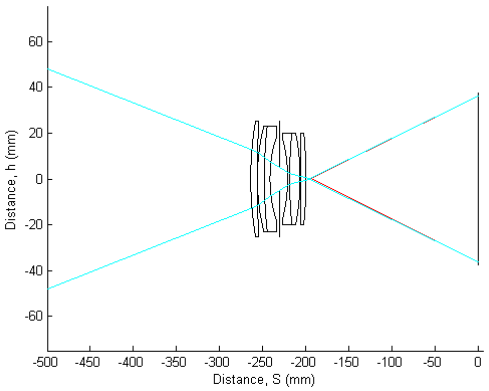

(a) Baseline

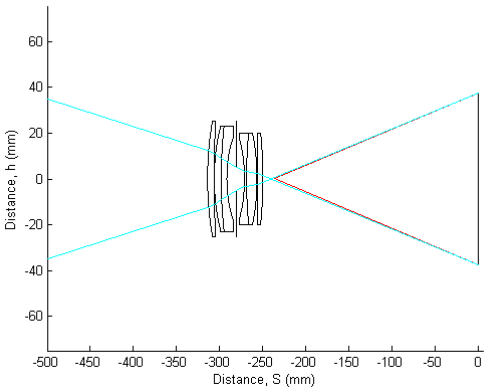

(b) Baseline + 50 mm

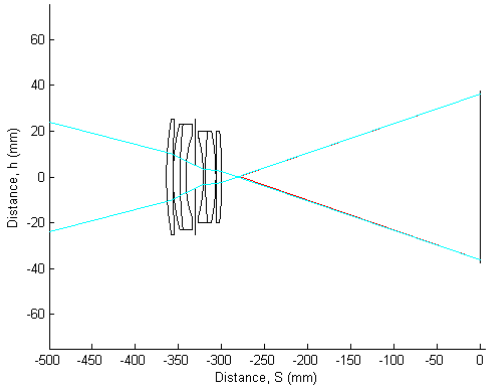

(c) Baseline + 100 mm

Figure 5.18: Effect of increasing image distance on focal point method

For the Nikkor lenses used in this experiment, the error between the known value and the calculated value increased as the image distance increased. This demonstrates that the value estimated by the focal point method is less than the back focal length, as is seen in Figure 5.18. Although the back focal length of the camera cannot be quantified, Eq. (5.5) shows that the rate of change in error should be linear when only the image distance of the lens is changed, which collaborates perfectly with the observed results.

To test the robustness of the correction for the focal point method, the exact same test was performed for a random image distance each day for five additional days. For the subsequent experiments, the focus of the lens was not held constant, but rather allowed to vary from day to day. For these tests, the magnification method was also performed

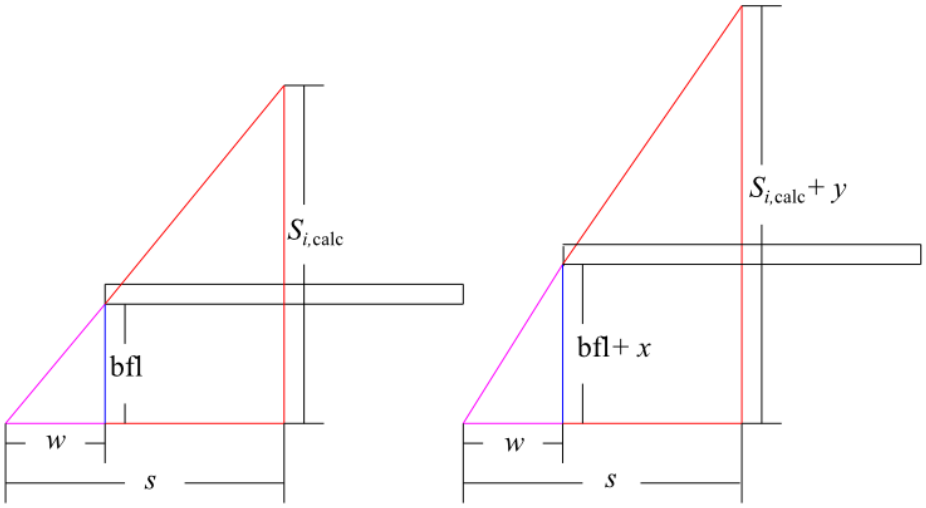

Figure 5.19: Effect of extension tube on focal point method.

to form a baseline for the expected results, since the image distance no longer correlated to the number of extension tubes directly when the focus of the lens is changed and the magnification method was already shown to have reliable results. As seen in Figures 5.20 and 5.21, there is a significant deviation in the accuracy of the focal point method on the later days. Table 5.5 shows the qualities of the error for both the original tests and for the subsequent days. Overall, for the original tests for the focal point method, the error is well within the desired region of accuracy, and shows comparable results to the magnification method.

This staunch difference between the original set of experiments and the later tests is attributed once again to the properties of a complex lens. The lenses used in this experiment use a rear focusing method to change the focus of the lens. Unlike some constant focal length lenses that shift the entire set of internal lenses forward to move the focal plane, a

Table 5.5: Accuracy of the focal point method compared with magnification

	50 mm			135 mm		
	Mag Method	Original	Later	Mag Method	Original	Later
Average	-0.730	-0.0007	-3.74	1.82	0.0098	38.95
Standard Dev	2.22	0.914	5.03	2.29	1.04	44.74
Max Error	4.51	1.82	-7.86	4.31	1.45	64.83

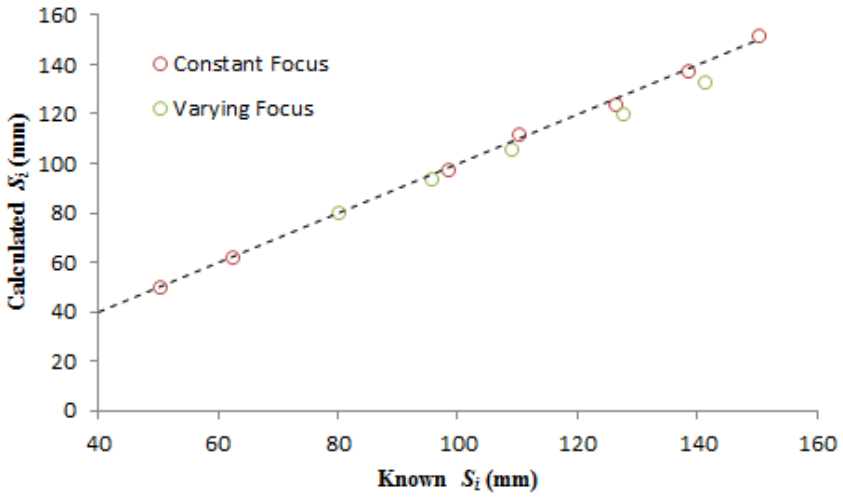

Figure 5.20: Image distance estimation robustness for a 50 mm lens.

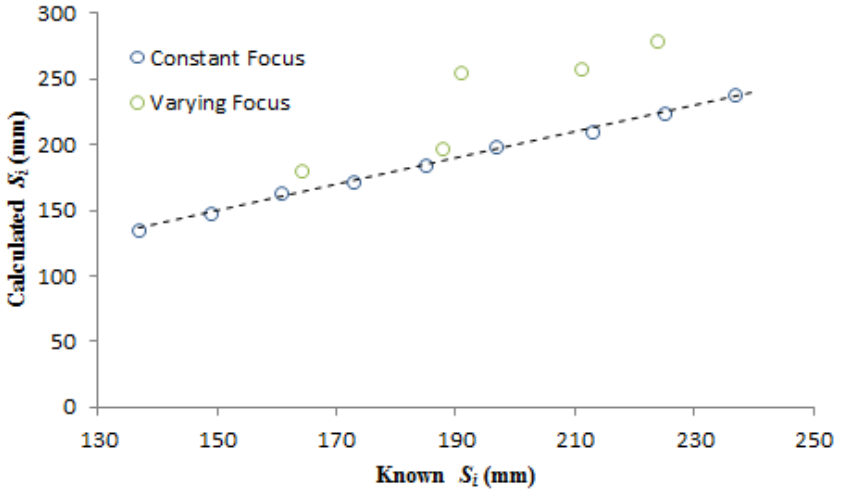

Figure 5.21: Image distance estimation robustness for a 135 mm lens.

rear focusing lens divides the internal lenses into groups and moves only the last set to alter the focus [30]. This method of focusing causes the focal length of the lens to be slightly altered with higher image distances, although the overall effect is minimized. When the rear element is moved instead of the full lens, the final angle of the light that exits the lens is changed, so that the last element does not have to move the same amount as the full lens would need to in order to obtain the same value of the image distance, as seen in Figure 5.22. Thus, the linear relationship obtained in Section 5.5 would not apply to the altered lens.

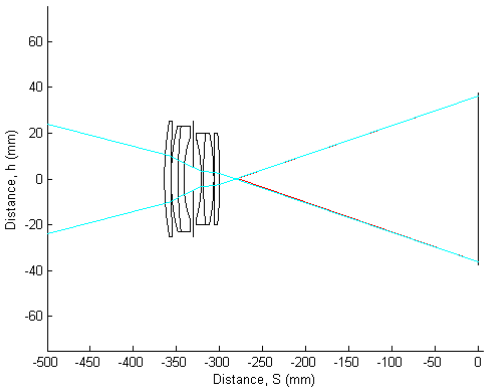

(a) Original element placement

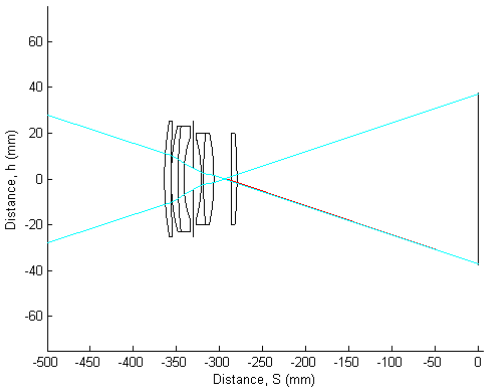

(b) Original + 10 mm

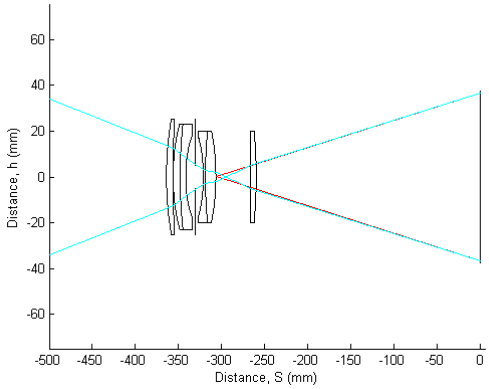

(c) Original + 20 mm

Figure 5.22: Effect of moving lens element on focal point method.

Chapter 6

Concluding Remarks

Based on geometry, the location of the centers of the focal points of the microlenses in a plenoptic camera should provide enough information to determine the image distance of the lens. In practice, however, the diversity of interfaces within both the camera itself and the lens were proven to cause unexpected errors in this relationship. First, the effects of refractive interfaces were examined to determine the impact on both reconstruction techniques and the estimation of the image distance of camera. It was shown that the reconstruction of the depths of objects in a plenoptic image was directly impacted by both forms of refractive interfaces, but the errors in depth caused by these interfaces could be corrected by a scale factor of the index of refraction of the surface. For the estimation of the image distance, the magnification method was shown to already account for these refractive effects, but the focal point method had to be adjusted in order to account for the thickness of the glass plate in front of the microlens array. Even with this adjustment, the experimental estimation of the image distance by the focal point method was shown to contain significant errors. This error was caused by the assumption that the light propagates in a straight line after passing through the aperture of the lens, when in reality the angle of propagation of the light was altered by several optical elements located after the aperture. The focal point calibration method in the current form is still capable of providing an estimation of the image distance with comparable accuracy to the magnification method. This process requires several steps and is detailed in Figure 6.1. If the optics of the lens after the aperture are changed in any way, this entire process must be repeated. For the lenses used in this experiment, which employed a rear focusing method for changing the magnification, only the last element of the lens moved, thus causing an error in approximation. For this reason, the magnification

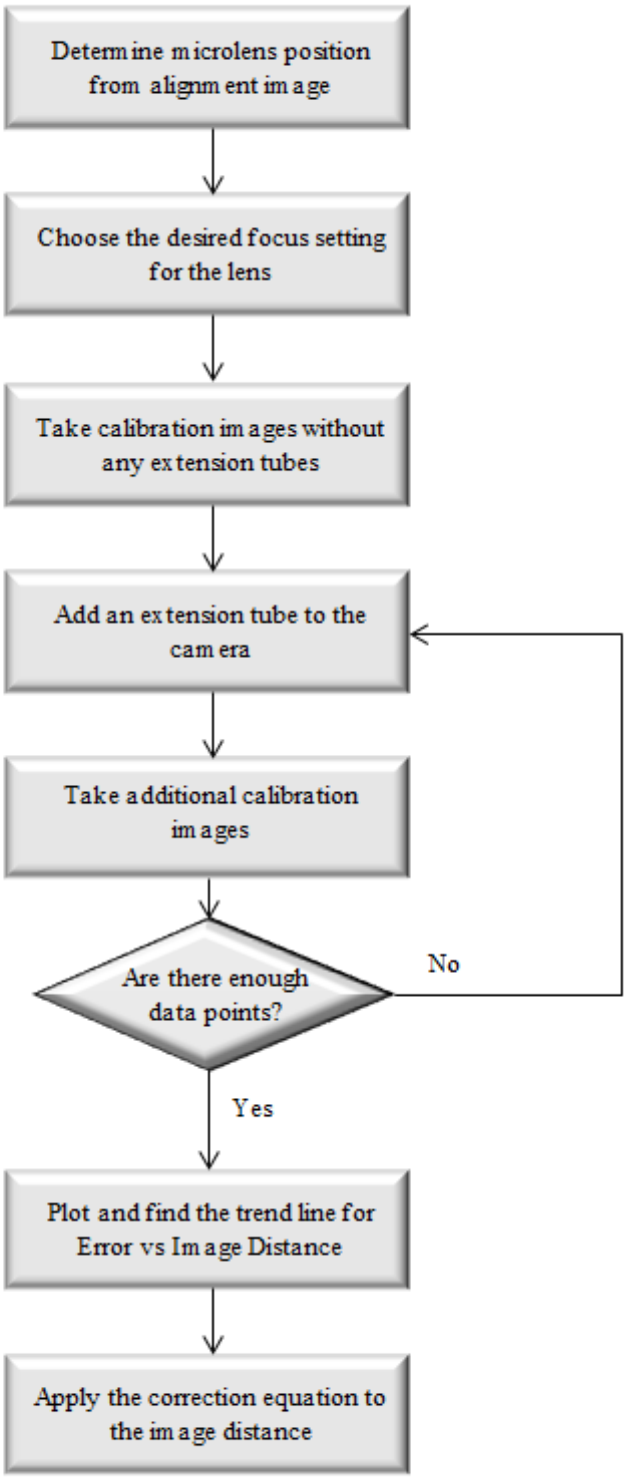

Figure 6.1: Focal point calibration process

method of calibration is currently the best method for determining the image distance, as it is much more simple to implement.

The focal point method of calibration does show the potential for further growth with more research. For the purposes of this research, the lens of the camera was modeled as a thin lens. Since the majority of the complications with this model were caused by the lens, improvements can be made where the lens is instead modeled by the actual elements of the lens. Should this new model also adapt to the shifts in the optical elements caused by a shift in the focus, the calibration steps detailed in Figure 6.1 would only be need to be performed when the microlens array is moved to properly eliminate the error in image distance induced by an imprecise alignment of the microlens array in the depth direction. The precise optics for a commercial lens are generally not disclosed to the public, so this next improvement to the focal point method may not be attainable. For best results with the current model, a lens with a constant focal length or a lens that is constantly set to focus at infinity could be used instead, both only changing the image distance through the use of extension tubes, which would allow a single calibration process to be applicable for a much wider range of experimental settings. At the time being, however, the focal point method of calibration should only be used when the magnification method is not easily implemented.

Bibliography

[1] Adrian, R., "Scattering Particle Characteristics and their Effect on Pulsed Laser Measurements of Fluid Flow: Speckle Velocimetry vs Particle Image Velocimetry," *Applied Optics*, Vol. 23, 1984, pp. 1690–1691.

[2] Adrian, R. and Westerweel, J., *Particle Image Velocimetry*, Cambridge University Press, 2011.

[3] Arroyo, M. and Greated, C., "Stereoscopic Particle Image Velocimetry," *Measurement Science and Technology*, Vol. 2, 1991, pp. 1181–1186.

[4] Raffel, M., Westerweel, J., Willert, C., and Gharib, M. an dKompenhans, J., "Analytical and Experimental Investigations of Dual-Plane Particle Image Velocimetry," *Optical Engineering*, Vol. 35, 1996, pp. 2067–2074.

[5] Ganapathisubramani, B., Longmire, E., Marusic, I., and Pothos, S., "Dual-Plane PIV Techinique to Determine the Complete Velocity Gradient Tensor in a Turbulent Boundary Layer," *Experiments in Fluids*, Vol. 39, 2005, pp. 222–231.

[6] Kahler, C. and Kompenhans, J., "Fundamentals of Multiple Plane Stereo Particle Image Velocimetry," *Experiments in Fluids*, Vol. 29, 2000, pp. S70–S77.

[7] Elsinga, G., Scarano, F., Wieneke, B., and van Oudheusden, B., "Tomographic Particle Image Velocimetry," *Experiments in Fluids*, Vol. 41, 2006, pp. 933–947.

[8] Belden, J., Truscott, T., Axiak, M., and Techet, A., "Three-Dimensional Synthetic Aperture Particle Image Velocimetry," *Measurement Science and Technology*, Vol. 21, 2010, pp. 125403:1–21.

[9] Willert, C., "Stereoscopic Digital Particle Image Velocimetry for Application in Wind Tunnel Flows," *Measurement Science and Technology*, Vol. 8, 1997, pp. 1465–1479.

[10] Brucker, C., "3-D Scanning-Particle-Image-Velocimetry: Technique and Application to a Sphereical Cap Wake Flow," *Applied Scientific Research*, Vol. 56, 1996, pp. 157–179.

[11] Hori, T. and Sakakibara, J., "High-Speed Scanning Stereoscopic PIV for 3D Vorticity Measurement in Liquids," *Measurement Science and Technology*, Vol. 15, 2004, pp. 1067–1078.

[12] Hinsch, K., "Holographic Particle Image Velocimetry," *Measurement Science and Technology*, Vol. 13, 2002, pp. R61–R72.

[13] Meng, H., Pan, G., Pu, Y., and Woodward, S., "Holographic Particle Image Velocimetry: from Film to Digital Recording," *Measurement Science and Technology*, Vol. 15, 2004, pp. 573–685.

[14] Ng, R., Levoy, M., Bredif, M., Duval, G., Horowitz, M., and Hanraham, P., "Light Field Photography with a Hand-held Plenoptic Camera," Str-ctsr 2005-02, Stanford University, Stanford, CA, 2005.

[15] Lynch, K., Fahringer, T., and Thurow, B., "Three-Dimensional Particle Image Velocimetry Using a Plenoptic Camera," *50th AIAA Aerospace Sciences Meeting Including the New Horizons Forum and Aerospace Exposition*, Nashville, TN, January 2012.

[16] Fahringer, T. and Thurow, B., "The Effect of Grid Resolution on the Accuracy of Tomographic Reconstruction Using a Plenoptic Camera," *51st AIAA Aersopace Sciences Meeting Including the New Horizons Forum and Aerospace Exposition*, Dallas, TX, January 2013.

[17] McCaffrey, J., *Easy Guide to Calibrating TEM's and STEM's*, Norrox Scientific Ltd., Ottawa, Canada.

[18] Lippmann, G., "La photographic intgrale." *Comptes-Rendus, Acadmie des Sciences*, Vol. 146, 1908, pp. 446–551.

[19] Adelson, E. and Bergen, J., "The Plenoptic Function and the Elements of Early Vision," *Computational Models of Visual Processing*, MIT Press, 1991.

[20] Adelson, E. and Wang, J., "Single Lens Stereo with a Plenoptic Camera," *IEEE Transactions on Pattern Analysis and Machine Intelligence*, Vol. 14, 1992, pp. 99–106.

[21] Gortler, S., Grzeszczuk, R., S. R., and Cohen, M., "The Lumigraph," Tech. rep., Microsoft Research, 1996.

[22] Levoy, M. and Hanrahan, P., "Light Field Rendering," Computer Science Department, Stanford University.

[23] Georgiev, T., Zheng, K., Curless, B., Salesin, D., Nayar, S., and Intwala, C., "Spatio-Angular Resolution Tradeoff in Integral Photography," *Eurographics Symposium on Rendering*, 2006.

[24] Lumsdaine, A. and Georgiev, T., "Ful Resolution LIghtfield Rendering," Tech. rep., Adobe Systems, Inc., 2008.

[25] Lynch, K., *Development of a 3-D Fluid Velocimetry Technique based on Light Field Imaging*, Master's thesis, Auburn University, 2011.

[26] Scarano, F. and Riethmuller, M., "Iterative Multigrid Approach in PIV Image Processing with Discrete WiWind Offset," *Experiments in Fluids*, Vol. 26, 1999, pp. 513–523.

[27] Fahringer, T. and Thurow, B., "Tomographic Reconstruction of a 3-D Flow Field Using a Plenoptic Camera," *42nd AIAA Fluid Dynamics Conference and Exhibit*, New Orleans, LA, June 2012.

[28] Bichal, A. and Thurow, B., "Development of a Background Oriented Schlieren Based Wavefront Sensor for Aero-Optics," *40th Fluid Dynamics Conference and Exhibit*, Chicago, IL, June 2010.

[29] Jenkins, F. and White, H., *Fundamentals of Optics*, McGraw-Hill Companies, Inc., 4th ed., 2001.

[30] Nikon Corperation, Fuji Bldg, Chiyoda-Ku, Tokyo, Japan, *AF DC-Nikkor 135mm f/2D Instruction Manual*.

[31] Smith, W., *Modern Optical Engineering*, McGraw-Hill Companies, Inc., 1966.

[32] Smith, W., *Modern Lens Design*, McGraw-Hill Companies, Inc., 2nd ed., 2005.

[33] Pokrajac, D. and Manes, C., "Velocity Measurements of a Free-Surface Turbulent Flow Penetrating a Porous Medium Composed of Uniform-Size Spheres," *Transport in Porous Media*, Vol. 78, 2009, pp. 367–383.

[34] Blois, G. e. a., "A Versatile Refractive-Index-Matched Flow Facility for Studies of Complex Flow Systems Across Scientific Disciplines," *50th AIAA Aerospace Sciences Meeting Including the New Horizons Forum and Aerospace Exposition*, AIAA, Nashville,TN, 2012.

Appendices

Appendix A

Refractive Index Matching Considerations

The reflection of light from a solid surface in a flow has been a clear problem in many recent PIV studies [33]. This reflection prevents accurate studies to be performed near the surface of an object, especially in the boundary layer. By matching the index of refraction of the fluid and the solid, light should pass unimpeded through both mediums, significantly reducing any surface reflection. The Refractive-Index Matching (RIM) Tunnel attempts to address the issue of surface reflection and obstruction interfering with the image quality near the surface of a model in a water tunnel.

A.1 Advantages of Index Matching

From the basic principles of Snell's law, light that passes though a change in the index of refraction is bent into a new direction of propagation [29]. Illumination of the flow is a requirement for all forms of PIV. For any experiment involving transparent models, the laser light impinging on the model may be either reflected or refracted in many directions, causing regions of high intensity in close proximity to the surface of the object. This scattering of light can be seen in Figure A.1(a). By matching the index of refraction between a model and the surrounding fluid, the light is able to pass straight through the model and the reflections are minimized. This is shown in Figure A.1(b). While this technique has many practical implications, one regime where a RIM Facility would be required is for porous flow. With the large density of solid model surfaces within the flow, large surface reflection would greatly reduce the already limited volume of fluid flow that could be studied. In addition to this, with a RIM Facility the flow behind a transparent model could be imaged without the

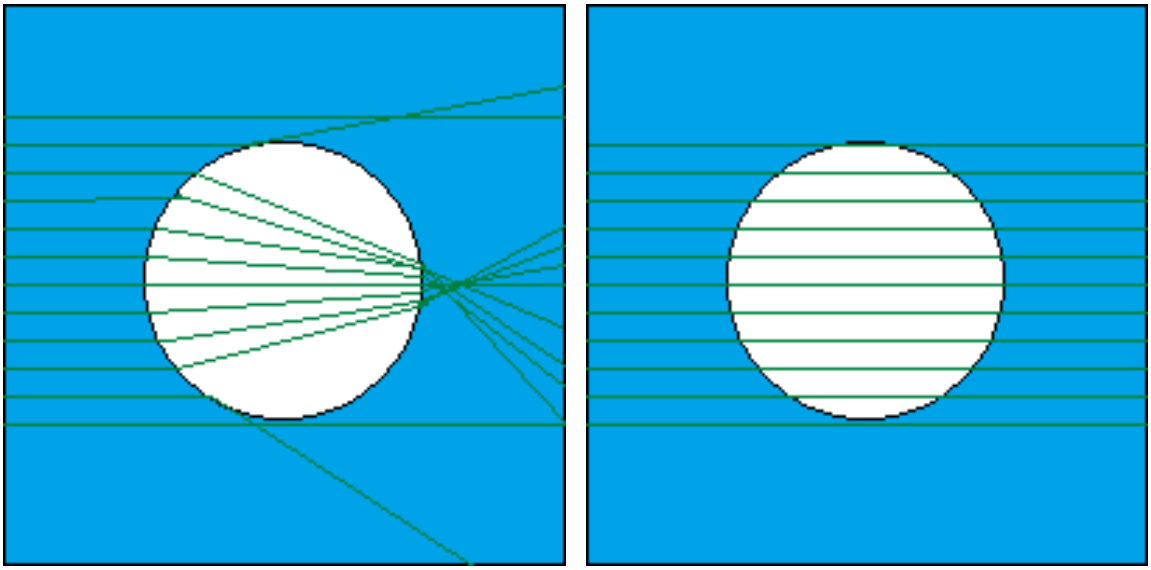

(a) Mismatched Indices (b) Matched Indices

Figure A.1: Light scattering due to refraction is corrected with index matching

distortion caused by the varying index. Flows could be examined closer to the middle of the test section rather than being focused on the region close to the wall.

A.2 Fluid and Solid Choice

Many considerations must be given to the solid/fluid combination that would be best suited for a given experiment. Ideally, the refractive index of the fluid should be between 1.33-1.6 to match most possible solid materials. While water can be used as a fluid within a RIM tunnel, the corresponding solids are often costly and difficult to manufacture. Other possible fluids propose unnecessary health or safety risks, or kinematic viscosities that would limit the range of Reynolds numbers that could be studied with the tunnel. Furthermore, the fluid should not chemically react with the index-matched solid. For the tunnel built by the University of Illinois, the fluid chosen was a 62.5% mixture of sodium iodide, NaI, and water, which has an index of refraction of 1.4947. The index of refraction for a liquid is dependent on the temperature of the fluid, but the index of refraction for NaI is relatively stable within the range of 20-30$°C$. The viscosity is approximately 10-15% greater than

Figure A.2: Current appearance of Auburn University water tunnel

pure water, which would allow flows of $Re > 10^5$ to be generated. This fluid matches the index of refraction of polymethyl methacrylate (PMMA), which is non-corrosive, simple to manufacture, and inexpensive. PMMA is also optically clear, transmitting 92% of visible light. While this combination appears perfect, this fluid choice comes with two significant drawbacks: NaI is highly corrosive and reacts with oxygen. Special care has to be taken in the design of the tunnel to ensure that all components are corrosion resistant, and the whole tunnel must be sealed against air to prevent contact with oxygen. To compensate, the tunnel built at the University of Illinois is pressurized with five psi of nitrogen [34].

A.3 RIM Facility Development

Within the past year, Auburn University has been developing a smaller version of the facility located at the University of Illinois, seen in Figure A.2. Due to the high corrosiveness of the sodium iodide solution, each part had to be manufactured with corrosion resistant materials. The test section has an area of 11.25 x 11.25 cm, a length of 30 cm, and is made of super abrasion-resistant (SAR) plexiglass. This plexiglass has the same index of refraction as PMMA, so that only the change in refraction between the tunnel wall and the outside

air will need to be considered in the imaging design. The converging section is fabricated from carbon fiber by technicians in Auburn's Polymer and Fiber Department. The main body of the converging section has an area 12.5 times larger than the test section, with a gently sloping nozzle. The other main components of the tunnel are made with high-density polyethylene (HDPE), such as the diverging section and the holder for the filters. The inner workings of the pump are also made of stainless steel to prevent corrosion. The pump is capable of pumping 100 gallons per minute, which should give a maximum flow velocity of approximately 0.6 m/s in the test section. This pump is connected to a variable frequency drive to control the velocity of the flow.

Due to the expense of sodium iodide, this tunnel was first tested with pure water to find any leaks. The pump was then run to examine the capabilities of the pump and flow regulator. The variable speed drive displays the current speed value, which is on a scale of zero to sixty units, to an accuracy of a tenth of a decimal. The exact velocity in the tunnel has not been measured at this point, but the desired maximum speed of 0.6 m/s was estimated to be reached well before the maximum setting. The next phase of the tunnel development will be to seal off the tunnel and connect the nitrogen pressurization system to the converging section of the tunnel.

Appendix B

Derivation of Relationship Equation

The relationship between a point on the microlens plane d and the corresponding focal point on the image sensor p is best related through the ray transfer matrices for optics [29]. The light entering through the center of the aperture first propagates through a constant medium for the distance l_3, as seen in Figure B.1. The index of refraction of the glass plate of the microlens array then causes the angle of the light to bend to a shallower angle, and this light then passes through the glass thickness t. Since a lens is designed such that light passing through the center of the lens does not change direction, the final portion of the propagation of a light ray is over the distance from the microlens plane to the sensor plane $\overline{f}$. In order to relate the two primary planes and eliminate unknown variables, the path of light was divided into two separate portions: from the main lens to the microlens plane, and then from the microlens plane to the image sensor.

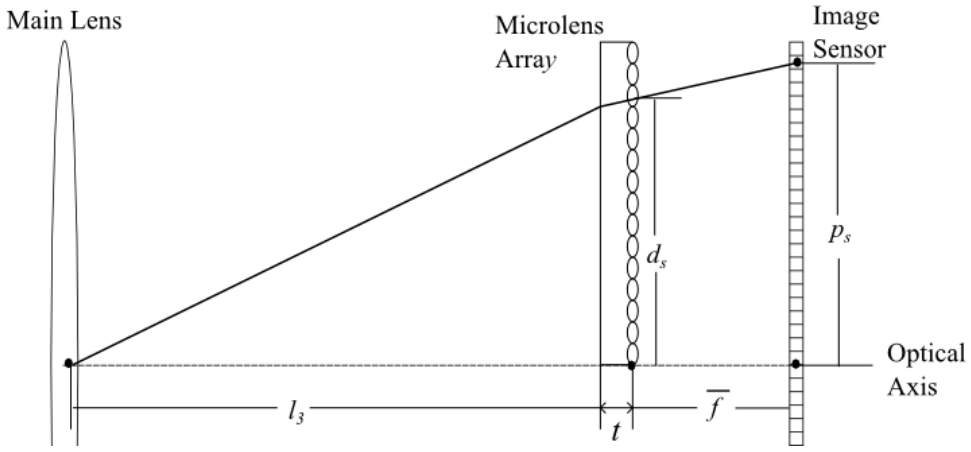

Figure B.1: Ray path through the plenoptic camera.

From the main lens to the microlens plane, the ray transfer matrices can be expressed in one dimension as

$$\begin{bmatrix} d_s \\ {}^{\theta}/_{n} \end{bmatrix} = \begin{bmatrix} 1 & t \\ 0 & 1 \end{bmatrix} \begin{bmatrix} 1 & 0 \\ 0 & {}^{1}/_{n} \end{bmatrix} \begin{bmatrix} 1 & l_3 \\ 0 & 1 \end{bmatrix} \begin{bmatrix} 0 \\ \theta \end{bmatrix} \tag{B.1}$$

Since the light entering the camera will always be from the center of the aperture for the microlens focal point image, the starting height for all light rays will be zero. The matrices can be combined into a singular square matrix, such that

$$\begin{bmatrix} d_s \\ {}^{\theta}/_{n} \end{bmatrix} = \begin{bmatrix} 1 & l_3 + {}^{t}/_{n} \\ 0 & {}^{1}/_{n} \end{bmatrix} \begin{bmatrix} 0 \\ \theta \end{bmatrix} \tag{B.2}$$

From the bottom portion of the matrices, it is clear that the change in angle is simply a factor of ${}^{1}/_{n}$. The change in height, however, is more complex, and can be extruded from the top portion of Eq. (B.2).

$$d_s = \left(l_3 + \frac{t}{n} \right) \theta \tag{B.3}$$

All variables in Eq. (B.3) are known except for the angle of propagation θ. For this reason, Eq. (B.3) can be solved for the angle of propagation so that θ can be determined from known quantities,

$$\theta = \left(\frac{n}{nl_3 + t} \right) d_s \tag{B.4}$$

The second portion of the ray transfer function, from the microlens plane to the sensor plane, only comprises of a single ray transfer matrix, such that

$$\begin{bmatrix} p_s \\ {}^{\theta}/_{n} \end{bmatrix} = \begin{bmatrix} 1 & \overline{f} \\ 0 & 1 \end{bmatrix} \begin{bmatrix} d_s \\ {}^{\theta}/_{n} \end{bmatrix} \tag{B.5}$$

During this portion, the light does not go through a change in propagation angle. Similar to the previous paragraph, the top portion of the matrix may be used to determine the change in height of the light between the array and the sensor. This is written as

$$p_s = d_s + \frac{\overline{f}\theta}{n} \tag{B.6}$$

Using Eq. (B.4) to substitute the angle of propagation for known values, Eq. (B.6) may be written as

$$p_s = d_s + \frac{\overline{f}}{n}\left(\frac{n}{nl_3 + t}\right) d_s \tag{B.7}$$

From here, the relationship equation may be simplified to the form presented in Chapter 4.

$$p_s = \left(1 + \frac{\overline{f}}{nl_3 + t}\right) d_s \tag{B.8}$$

While this derivation is only shown in the s dimension, the exact same equation is true for relating d_t to p_t.